

The CARM1 transcriptome and arginine methylproteome mediate skeletal muscle integrative biology



Tiffany L. vanLieshout¹, Derek W. Stouth¹, Nicolas G. Hartel², Goutham Vasam³, Sean Y. Ng¹, Erin K. Webb¹, Irena A. Rebalka⁴, Andrew I. Mikhail¹, Nicholas A. Graham², Keir J. Menzies^{3,5}, Thomas J. Hawke⁴, Vladimir Ljubicic^{1,*}

ABSTRACT

Objective: Coactivator-associated arginine methyltransferase 1 (CARM1) catalyzes the methylation of arginine residues on target proteins to regulate critical processes in health and disease. A mechanistic understanding of the role(s) of CARM1 in skeletal muscle biology is only gradually emerging. The purpose of this study was to elucidate the function of CARM1 in regulating the maintenance and plasticity of skeletal muscle.

Methods: We used transcriptomic, methylproteomic, molecular, functional, and integrative physiological approaches to determine the specific impact of CARM1 in muscle homeostasis.

Results: Our data defines the occurrence of arginine methylation in skeletal muscle and demonstrates that this mark occurs on par with phosphorylation and ubiquitination. CARM1 skeletal muscle-specific knockout (mKO) mice displayed altered transcriptomic and arginine methylproteomic signatures with molecular and functional outcomes confirming remodeled skeletal muscle contractile and neuromuscular junction characteristics, which presaged decreased exercise tolerance. Moreover, CARM1 regulates AMPK-PGC-1 α signalling during acute conditions of activity-induced muscle plasticity.

Conclusions: This study uncovers the broad impact of CARM1 in the maintenance and remodelling of skeletal muscle biology.

© 2022 The Author(s). Published by Elsevier GmbH. This is an open access article under the CC BY-NC-ND license (<http://creativecommons.org/licenses/by-nc-nd/4.0/>).

Keywords AMPK; PGC-1 α ; Muscle plasticity; Mitochondria; Neuromuscular junction

1. INTRODUCTION

Coactivator-associated arginine methyltransferase 1 (CARM1) is part of a family of protein arginine methyltransferase (PRMT) enzymes that catalyze the methylation of arginine residues on target proteins. This posttranslational modification regulates several critical cell processes, such as RNA metabolism, development and differentiation, and autophagy [1–4]. It is not surprising therefore that dysregulation of CARM1 (also known as PRMT4) expression or activity has been implicated in a variety of health disorders including cancer, as well as neurodegenerative and cardiovascular diseases [5–7]. As such, advancing our understanding of this methyltransferase from bench to bedside, including its therapeutic targeting [8–11], may be useful for discovering and developing treatment strategies.

CARM1 is also emerging as an important regulator of skeletal muscle biology, a dynamic tissue accounting for 30–40% of body mass that is essential for metabolism, respiration, and mobility [12]. Indeed, we [13–19] and others [20–25] have shown that CARM1 expression and activity are altered during conditions of muscle plasticity and that the

methyltransferase is required for myogenesis, glucose metabolism, and the maintenance and remodelling of muscle mass. In particular, recent work has highlighted CARM1-mediated autophagic and atrophic signalling in skeletal muscle [15,19,24–26], revealing a mechanism by which CARM1 influences AMP-activated protein kinase (AMPK) and its downstream network to affect muscle mass. However, while recent, very elegant studies have described the arginine methylproteome in several cell types [27–31], arginine methylation in skeletal muscle is largely unexplored, including the arginine methyltransferase activity of CARM1. Furthermore, the specific role of CARM1 in regulating skeletal muscle gene expression, morphology, and function also remains undefined.

To further investigate the *in vivo* relevance of CARM1 in skeletal muscle, in this study we used CARM1 skeletal muscle-specific knockout (mKO) mice [19] and a broad experimental approach that includes a novel arginine methylproteomic strategy along with complementary transcriptomic, molecular, and physiological methodologies. We show that the prevalence of arginine methylation in skeletal muscle is similar to other essential posttranslational modifications, like phosphorylation and

¹Department of Kinesiology, McMaster University, Hamilton, ON, L8S 4L8, Canada ²Mork Family Department of Chemical Engineering and Materials Science, University of Southern California, Los Angeles, CA, 90089, USA ³Interdisciplinary School of Health Sciences, Faculty of Health Sciences, University of Ottawa, Ottawa, ON, K1H 8M5, Canada ⁴Department of Pathology and Molecular Medicine, McMaster University, Hamilton, ON, L8S 4L8, Canada ⁵Ottawa Institute of Systems Biology and the Centre for Neuromuscular Disease, Department of Biochemistry, Microbiology and Immunology, University of Ottawa, 451 Smyth Rd, K1H 8M5, Ottawa, Canada

*Corresponding author. E-mail: ljubicic@mcmaster.ca (V. Ljubicic).

Received January 11, 2022 • Revision received July 14, 2022 • Accepted July 15, 2022 • Available online 21 July 2022

<https://doi.org/10.1016/j.molmet.2022.101555>

ubiquitination. We also reveal that CARM1 mKO mice have a modified transcriptomic profile, which portends altered skeletal muscle contractile and neuromuscular junction (NMJ) characteristics and decrements in integrative physiology, such as decreased exercise capacity. Finally, we demonstrate that CARM1 regulates AMPK-peroxisome proliferator-activated receptor γ coactivator-1 α (PGC-1 α) signalling during acute conditions of muscle adaptive plasticity, which extends earlier work [17,19,24,25]. To our knowledge, this study represents the most comprehensive investigation of CARM1 in muscle and our data underscore the emerging relevance of this arginine methyltransferase to skeletal muscle biology.

2. MATERIALS AND METHODS

2.1. Mouse model and genotyping

CARM1 mKO were engineered as previously reported [19] using the Cre/loxP system. CARM1 floxed animals [32,33] were a gift from Dr. Mark Bedford (The University of Texas MD Anderson Cancer Centre, Smithville, TX, USA) and were generated in the mixed C57BL6J/129 background. These mice were then crossed with human α -skeletal actin (HSA)-Cre mice obtained from Jackson Laboratories (Bar Harbor, ME, USA). Through DNA extracted from tail tissue, littermates were identified as either floxed CARM1 wildtype (WT) or CARM1 mKO animals using RT-PCR and gel electrophoresis techniques. For these studies, 12-week-old, male WT and mKO mice were housed in an environmentally controlled room (23 °C, 12 h light/12 h dark cycle) and provided food and water ad libitum at the Central Animal Facility at McMaster University. We exclusively used male animals in order to better compare our findings to existing literature [13,15,17,19,22,24,26]. All protocols were approved by the University Animal Research Ethics Board operating under the auspices of the Canadian Council for Animal Care.

2.2. Evaluation of integrative physiology

Ambulatory activity was measured using an open-field Opto-Varimex-5 Auto-Track (Columbus Instruments, Columbus, USA) as previously described [34]. All mice were acclimatized to the position tracking chamber 48 and 24 h prior to the testing day by undergoing a 5 min session in the open field chamber. On the testing day mice underwent a 1 h data collection session in a quiet environment without disruption. A variety of activity measures were recorded, including distance travelled, average speed, ambulatory time, stereotypic time, rearing events, and time spent in the center or edge of the chamber.

The pen test examined mice for motor function performance [35]. For this test, mice were placed on a pen and the time that a mouse remained balanced was recorded. Familiarization was performed 48 and 24 h prior to data collection. On the testing day the mice performed 3 trials and the best time (i.e., longest duration before falling) of these 3 trials was used for statistical analysis. If a mouse fell off within 3 s of being placed on the pen, the test was restarted, and that trial was not counted. 60 s was set as the test ceiling.

Rotarod testing was performed as previously described [36]. All mice were acclimatized to the rotarod machine 48 and 24 h prior to data collection. During data collection the mouse was placed on the rotarod, which accelerated from 5 to 45 rpm over 300 s, followed by an additional 300 s at 45 rpm. The time and speed at failure was recorded. The test was performed 3 times for each animal and the best of these trials was used for statistical analysis.

Mice also underwent forelimb and all limb grip strength measurements [36] by pulling on a grid-grip dynamometer (Columbus Instruments, Columbus, USA). Familiarization was performed 48 and 24 h prior to

data collection, where mice completed 1 set containing 3 repetitions of the outlined protocol below. On the testing day each mouse performed 3 successive pull attempts and was then returned to their cage for a rest period of 1 min. This was repeated 5 times, for a total of 15 attempts. Maximum grip strength was determined by taking the average of the 3 highest successive values out of the 15 pulls recorded and normalizing to body weight in grams. Fatigue was determined by calculating the decrement between the average of the first 2 series of attempts (1 + 2 + 3 = A, 4 + 5 + 6 = B) and the last 2 series of pulls (10 + 11 + 12 = C, 13 + 14 + 15 = D) using formula (C + D)/(A + B).

For acute exercise, animals were randomly assigned to one of three experimental groups: 1) sedentary (SED) animals euthanized by cervical dislocation while at rest, 2) mice challenged with a single bout of exercise on a motor-driven rodent treadmill (Columbus Instruments, Columbus, OH) that were killed and had their tissues collected immediately, OAE, and 3) mice that ran and were killed 3 h following the end of the treadmill challenge, 3AE. Mice in both the OAE and 3AE groups were acclimatized to the treadmill (i.e., 5 m/min for 10 min) 48 and 24 h prior to the beginning of the experiment (and 48 h after functional test performance). The exercise protocol began at 15 m/min and increased by 5 m/min at the 10 and 20 min marks. The incline began at 5° and increased by 5° at the 30, 40 and 70 min marks. If mice could continue running beyond 90 min, the speed was increased by 5 m/min every 5 min until exhaustion, which was determined by probing the mice with a soft bristle brush for 5 s once mice stopped running. If the mice did not restart running following this prompt, they were determined to be exhausted [37]. During tissue collection, the tibialis anterior (TA), extensor digitorum longus (EDL), soleus (SOL), gastrocnemius (GAST), quadriceps (QUAD), and triceps (TRI) muscles from the left and right limbs were rapidly excised, weighed, frozen in liquid nitrogen or mounted in optimum cutting temperature (OCT) compound (Thermo Fisher Scientific Life Sciences, Waltham, MA, USA) then frozen in isopentane cooled with liquid nitrogen. All muscles were then stored at -80 °C for biochemical analysis.

Examination of integrative physiology was performed as follows to minimize functional impact between tests: forelimb grip strength, open field test, all limb grip strength, pen test, rotarod test, and 48 h later the acute exercise challenge.

2.3. In situ muscle contraction

In situ muscle functional testing was performed using a whole-mouse test system (model 1300A, Aurora Scientific Inc., Aurora, ON, Canada). Briefly, animals were anaesthetized via intraperitoneal ketamine/xylazine injection. The GAST/plantaris/SOL complex (GPS) of the right hindlimb was isolated from its distal insertion, keeping nerve and vasculature intact, and the calcaneal tendon, anchored by the calcaneus, was distally secured to a force transducer (model 809c, Aurora Scientific Inc.). The muscle was stimulated via the sciatic nerve (within the gluteal region; cleared of connective tissue and proximally severed) using platinum-coated electrodes. Optimal stimulation voltage and muscle length were determined as previously described [38,39].

A force-frequency curve was used to determine peak tetanic force before (pre-) and after (post-) a muscle-fatiguing protocol. This force determination consisted of a 1 s stimulation every 30 s beginning at 10 Hz and increasing in stimulation frequency in 10 Hz increments. The fatigue protocol, eliciting maximal tetanic contractions within the GPS, consisted of 5 min of 100 millisecond/100 Hz stimulations in 1 s trains followed by 5 min of 300 millisecond/100 Hz stimulations in 400 ms trains, as previously reported [40,41]. A twitch contraction was

performed before the fatigue protocol to ascertain maximum twitch force, time to peak twitch, maximum rates of force production and relaxation, and half relaxation time.

All data were collected and analysed via the Dynamic Muscle Control and Analysis Software (version 615A, Aurora Scientific Inc.). Following muscle stimulation, hindlimb muscles were removed and stored for subsequent analysis.

2.4. Whole muscle protein extraction and quantification

A small portion of TA muscles (~15–25 mg) was added to a 2 mL ppendorf tube with a pre-determined volume of RIPA buffer (Sigma–Aldrich, St. Louis, Missouri, USA, MO; 20 µL of RIPA per 1 mg muscle weight) supplemented with a protease and phosphatase inhibitor cocktail (Roche, Laval, Quebec, Canada). 1 stainless steel ball bearing was added to the tube with care being taken to ensure that the samples were kept on ice throughout the entire extraction process. The tube was loaded into a pre-cooled Phillips Homogenizer (Qiagen, Toronto, Ontario, Canada) and run for 3–5 bouts of 40 s at a frequency of 20.0 1/second. The ball bearing was then removed using clean tweezers, and samples were placed in a fast prep machine (MP Bio-medicals, Solon, Ohio, United States) at 6.0 m/s for 40 s. The tubes were then rolled end-over-end for 1 h at 4 °C. Following this samples were spun in a centrifuge at 14,000 g for 10 min at 4 °C. The resulting supernates were then collected and aliquoted into new 1.5 mL ppendorf tubes. A bicinchoninic assay (BCA; ThermoFisher Scientific, BioTek, Toronto, Ontario) was performed to determine protein concentration.

2.5. Western blotting

20 µg of protein was loaded into each lane of 4–15% polyacrylamide gels and subjected to SDS-PAGE, before being transferred to nitrocellulose membranes. After transfer, Ponceau S solution (Sigma, Darmstadt, Germany) was used to verify equal loading across all lanes [42]. Ponceau solution was washed off with Tris-buffered saline with 1% Tween-20 (TBS-T). Membranes were then blocked with 5% milk for 60 min before being washed 5 × 3 min with TBS-T. Primary antibody dilutions were prepared in 5% milk or bovine serum albumin (BSA) as per manufacturer's recommendations. The following antibodies were used: CARM1 (1:5000; A300-421A; Bethyl Laboratories, Montgomery, Texas, USA), MMA (8015, Cell Signaling, Danvers, MA, USA), SmBme0 (1:1,000; SAB2102256; Millipore Sigma, Etobicoke, ON, Canada), PRMT1 (1:5,000; 07–404; EMD Millipore, Darmstadt, HE, Germany), PRMT5 (1:1,000; 507–405; EMD Millipore), PRMT6 (1:5,000; A300-929A; Bethyl laboratories), PRMT7 (1:100; Sc-376077; Santa Cruz, Santa Cruz, CA, USA), BAF155me2a (1:1,000; 94962; Cell Signaling), BAF155 (1:150; 11956S; Cell Signaling), PABP1me2a (1:1,000; 3505S; Cell Signaling), PABP1 (1:1,000; 4992S; Cell Signaling), CARM1 substrate (1:1,000; a kind gift from Dr. Mark Bedford, MD Anderson Cancer Center, University of Texas [18,19,43], ADMA at glycine and arginine-rich sequences (1:200; 13522; Cell Signaling), SDMA (1:200; 13222; Cell Signaling), total OXPHOS (1:1,000; ab110413; Abcam, Cambridge, UK), phosphorylated AMPK (1:1,000; 2535S; Cell Signaling), AMPK (1:1,000; 2532S; Cell Signaling), and PGC-1α (1:1,000; AB3242; EMD Millipore). Primary antibodies were applied overnight at 4 °C with gentle shaking and washed off the following morning with 5 × 3 min washes in TBS-T. Appropriate horseradish peroxidase linked secondary antibodies were applied for 2 h at room temperature followed by 5 × 3 min washes in TBS-T. Finally, enhanced chemiluminescence substrate

(Bio-Rad, Mississauga, Ontario, Canada) was applied to detect target proteins. Images were captured with ChemiDoc MP Imaging System (Bio-Rad) and Image Lab (Bio-Rad) was employed for densitometry.

2.6. RNA isolation and real-time polymerase chain reaction (RT-qPCR)

Total RNA was isolated from frozen EDL and SOL muscles, as described previously [19]. All samples were homogenized in 1 mL of Trizol reagent (Invitrogen, Carlsbad, CA, USA) using stainless steel lysing beads and TissueLyser (Qiagen, Hilden, NRW, Germany) run for 40 s at a frequency of 20.0 1/second. Homogenized samples were then mixed with 200 µL of chloroform (Thermo Fisher Scientific, Waltham, MA, USA), agitated vigorously for 15 s and centrifuged at 12,000 g for 10 min. The upper aqueous (RNA) phase was purified using the Total RNA Omega Bio-Tek kit (VWR International, Radnor, PA, USA) as per the instructions provided by the manufacturer. RNA concentration and purity were determined using the NanoDrop 1000 Spectrophotometer (Thermo Fisher Scientific Life Sciences, Waltham, MA, USA). RNA samples were then reverse-transcribed into cDNA using a high-capacity cDNA reverse transcription kit (Thermo Fisher Scientific Life Sciences, Waltham, MA, USA) according to the manufacturer instructions. All individual RT-qPCRs were run in triplicate 6 µL reactions containing GoTaq qPCR Master Mix (Promega, Madison, WI, USA). Data were analyzed using the comparative CT method [44]. 18S ribosomal RNA (18S) was used as a control housekeeping gene for all experiments, as the CT values for this gene did not change between experimental groups (data not shown). The following primers were used in this study: CARM1 F-CAACAGCGTCTCATCCAGT, R-GTCCGCTCACT-GAACACAGA; PRMT1 F-ACCCTCACATACCGAACTC, R-TGTTGGCTTT GACAATCTTCAC; PRMT5 F-TCTCCCCACCAGCATTTTCC, R-TGGAGGGC-GATTTTGGCTTA; PRMT7 F-AAATGGACCCTGAGGGCAAG, R-CGGCAGGAA GTACACACACT; cholinergic receptor nicotinic alpha 1 subunit (CHRNA1) F-TCCCTTCGATGAGCAGAACT, R-GGGCAGCAGGAGTAGAACAC; forkhead box O1 (FOXO1) F-GCTGGGTGTGTCAGGCTAAGAG, R-GAGGGGTGAAGGG-CATCT; cholinergic receptor nicotinic gamma subunit (CHRNA3) F-GCTCA GCTGCAAGTTGATCTC, R- CCTCCTGCTCCATCTCTGTG; fibroblast growth factor binding protein 1 (FGFBP1) F-ACACTCACAGAAAGGTGTCCA, R-CTG AGAAGCCTGAGTAGCC; PGC-1α F- GGTGTAGCGACCAATCGGAA, R-TCA CCAAACGCACGTCAGTA; 18S F-AGTTAGCATGCCAGAGTCTGC, R-TGCAT GGCCGTTCTTAGTTG.

2.7. RNA Purification and library preparation

10–15 mg of powdered frozen muscle tissue was manually homogenized in Trizol (Invitrogen) and total RNA was purified using a standard chloroform extraction using the manufacturer's protocol. Total RNA samples were quantified using Qubit HS RNA assay (Thermo) and fragment size was evaluated using the Fragment Analyzer HS NGS assay (AATI). RNA Quality Number (RQN) of 8.0 or higher is considered satisfactory quality for library construction. Library construction was performed with the Truseq RNA v2 (Illumina). Libraries were prepared with unique barcodes compatible with the Illumina NextSeq 500 platform. Quantification of the libraries were performed with the Qubit HS DNA assay (Thermo) and library fragment size was evaluated with the Fragment Analyzer HS NGS assay (AATI). Libraries were normalized to the same concentration, then samples were pooled in equal amounts.

2.8. RNA sequencing and analysis

The library pool was diluted as required to achieve maximal cluster density and run on one High Output Flow Cell on the NextSeq 500. PhiX

was spiked in as a control. Samples underwent 1 x 75 cycles of single-end sequencing, which yielded approximately 50 million reads per sample prior to filtering. Analysis was performed using the applications on BaseSpace Sequence Hub (Illumina). Raw reads were aligned to the genome and transcriptome of *Mus musculus* (build mm10) using RNA-Seq Alignment (BaseSpace Workflow) v1.1.1 application [45]. Differential expression was analyzed using a t-test of log-transformed FPKM values and adjusted for multiple testing using a Benjamini-Hochberg q-value [46] by launching the Cufflinks Assembly and DE (BaseSpace Workflow) v2.1.0. Over-representation GO pathway analyses were performed using GO enrichment analysis powered by Panther [47]. The data discussed in this publication have been deposited in NCBI's Gene expression Omnibus [48] and are accessible through GEO Series accession number GSE189351 (<https://www.ncbi.nlm.nih.gov/geo/query/acc.cgi?acc=GSE189351>).

2.9. Correlation Engine

Illumina BaseSpace™ Correlation Engine (BSCE, Illumina, San Diego, CA, <https://sapac.illumina.com/products/by-type/informatics-products/basespace-correlation-engine.html>), a platform with publicly available genomic knowledge, was used to validate our results and find associations by matching and integrating our transcriptomic data. The differentially expressed geneset was used as the input bioset and correlated to more than 142,219 ontologically tagged biosets comprising more than 23,529 curated studies [49] as of September, 2019. The bioset data stored in the BSCE goes through various levels of pre-processing, quality control and organization. Quality controls ensure the integrity of samples and datasets and include boxplot evaluations before and after normalization, missing value counts, and p-value histograms after statistical testing with a false discovery rate analysis to determine if the number of genes significantly changed is greater than the number expected by chance.

BSCE implemented a rank-based non-parametric Running Fisher algorithm to compare the CARM1 mKO vs WT mice transcriptome dataset with other transcriptomic biosets in the database. The Running Fisher algorithm calculates the statistical significance of the similarity between ranked fold change values of the 2 biosets in comparison using a Fisher's exact test. This approach allows for comparability across data from different studies, platforms, and analysis methods. BSCE Disease Atlas was used to identify highly correlated musculoskeletal diseases based on the bioset–bioset correlations of disease vs. normal experimental designs (31,955 biosets) and associated phenotype tags. The BSCE Meta-Analysis application was used to aggregate, score and rank genes across the CARM1 mKO vs WT bioset and select highly ranked musculoskeletal disease biosets in BSCE curated studies to assess common and differential RNA expression activities.

2.10. Whole cell lysate

QUAD muscle tissues were lysed by probe sonication in 8 M urea, 50 mM Tris–HCl pH 7.5, 1 mM activated sodium vanadate, 2.5 mM sodium pyrophosphate, 1 mM β-glycerophosphate and 100 mM sodium phosphate. Insoluble cell debris were filtered by 0.22 μm syringe filter. Protein concentration was measured with a BCA assay (Pierce, PI23227). Lysates were reduced with 5 mM DTT, alkylated with 25 mM iodoacetamide, quenched with 10 mM DTT, and acidified to pH 2 with 5% trifluoroacetic acid. Proteins were then digested to peptides using a 1:100 trypsin-to-lysate ratio by weight. Tryptic peptides were desalted by reverse phase C18 StageTips and eluted

with 30% acetonitrile. 1 mg of peptide was saved for high pH SCX enrichment and 5 mg were saved for immunoaffinity enrichment. The eluents were vacuumed dried, and 750 nanogram/injection was submitted to LC-MS.

2.11. High pH strong cation exchange (SCX)

As previously described [50], 1 mg of digested protein was resuspended in loading buffer (60% acetonitrile, 40% BRUB (5 mM phosphoric acid, 5 mM boric acid, 5 mM acetic acid, pH 2.5) and incubated with high pH SCX beads (Sepax, Newark, DE) for 30 min, washed with washing buffer (80% acetonitrile, 20% BRUB, pH 9), and eluted into 3 fractions using elution buffer 1 (60% acetonitrile, 40% BRUB, pH 9), elution buffer 2 (60% acetonitrile, 40% BRUB, pH 10), elution buffer 3 (60% acetonitrile, 40% BRUB, pH 11). Eluates were dried, resuspended in 1% trifluoroacetic acid and desalted on STAGE tips with 2 mg of HLB material (Waters) loaded onto 300 μl tip with a C8 plug (Empore, Sigma, St. Louis, MO).

2.12. Immunoaffinity purification (IAP)

5 mg of digested proteins were dissolved in 1X immunoprecipitation buffer (50 mM MOPS, 10 mM Na₂HPO₄, 50 mM NaCl, pH 7.2, Cell Signaling). Modified SDMA peptides, ADMA peptides, and MMA peptides were immunoprecipitated by addition of 40 μl of PTMScan Symmetric Di-Methyl Arginine Motif Kit (13563, Cell Signaling), PTMScan Asymmetric Di-Methyl Arginine Motif Kit (13474, Cell Signaling), and PTMScan Mono-Methyl Arginine Motif Kit (12235, Cell Signaling), respectively. Lysates were incubated with PTMScan motif kits for 2 h at 4 °C on a rotator. Beads were centrifuged and washed 2 times in 1X immunoprecipitation buffer followed by 3 washes in water, and modified peptides were eluted with 2 × 50 μl of 0.15% TFA and desalted on STAGE tips with C18 cores (Empore, Sigma). Enriched peptides were resuspended in 50 mM ammonium bicarbonate (Sigma) and subjected to a second digestion with trypsin for 2 h per the manufacturer's recommendation, acidified with trifluoroacetic acid to pH 2 and desalted on STAGE tips.

2.13. Mass spectrometric analysis

All LC-MS experiments were performed on a nanoscale UHPLC system (EASY-nLC1200, Thermo Scientific) connected to an Q Exactive Plus hybrid quadrupole-Orbitrap mass spectrometer equipped with a nano-electrospray source (Thermo Scientific). Peptides were separated by a reversed-phase analytical column (PepMap RSLC C18, 2 μm, 100 Å, 75 μm × 25 cm) (Thermo Scientific). For whole cell lysates flow rate was set to 250 nl/min at a gradient from 3% buffer B (0.1% formic acid, 80% acetonitrile) to 38% B in 110 min, followed by a 10 min washing step to 85% B. For high pH SCX the flow rate was set to 250 nl/min at a gradient starting with 0% buffer B to 29% B in 142 min, then washed by 90% B in 10 min, and held at 90% B for 3 min. The maximum pressure was set to 500 bar and column temperature was constant at 55 °C. For IAP samples the flow rate was set to 250 nl/min at a gradient starting with 0% buffer B to 25% B in 132 min, then washed by 90% B in 10 min. Dried SCX fractions were resuspended in buffer A and injected as follows, E1: 1.5 μl/60 μl, E2–4: 5 μl/6 μl. IAP samples were resuspended in 7 μl and 6.5 μl was injected. The effluent from the HPLC was directly electrosprayed into the mass spectrometer. Peptides separated by the column were ionized at 2.0 kV in the positive ion mode. MS1 survey scans for DDA were acquired at resolution of 70k from 350 to 1,800 m/z, with maximum injection time of 100 ms and AGC target of 1e6. MS/MS

fragmentation of the 10 most abundant ions were analyzed at a resolution of 17.5k, AGC target 5e4, maximum injection time 120 ms for IAP samples, 240 ms for SCX samples, 65 ms for whole cell lysate samples, and normalized collision energy 32. For whole cell lysates the normalized collision energy was set to 26. Dynamic exclusion was set to 30 s and ions with charge 1 and > 6 were excluded. The mass spectrometry proteomics data have been deposited to the ProteomeXchange Consortium via the PRIDE partner repository with the dataset identifier PXD028884 [51].

2.14. Identification and quantitation of peptides

Tandem mass spectrometry (MS/MS) fragmentation spectra were searched with Proteome Discoverer SEQUEST (version 2.2, Thermo Scientific) against the in-silico tryptic digested Uniprot Mus Musculus database with all reviewed with isoforms (release Jun 2017). The maximum missed cleavage rate was set to 4. Trypsin was set to cleave at R and K. Dynamic modifications were set to include monomethylation of arginine or lysine (R/K, +14.01565), di-methylation of arginine or lysine (R/K, +28.0313), tri-methylation of lysine (K, +42.04695), oxidation on methionine (M, +15.995 Da, and acetylation on protein N terminus (+42.011 Da). Fixed modification was set to carbamidomethylation on cysteine residues (C, +57.021 Da). The maximum parental mass error was set to 10 ppm and the MS/MS mass tolerance was set to 0.02 Da. Peptides with sequence of 6–50 amino acids were considered. Methylation site localization was determined by ptm-RS node in Proteome Discoverer, and only sites with localization probability greater or equal to 75% were considered. The FDR threshold was set strictly to 0.01 using Percolator node validated by q-value. Relative abundances of parental peptides were calculated by integration of area-under-the-curve of the MS1 peaks using Minora LFQ node in Proteome Discoverer 2.2. The Proteome Discoverer export peptide groups abundance values were log2 transformed, normalized to the corresponding samples median values, and significance was determined using a t-test permutation-based approach in the Perseus environment (release 1.6.2.3) to generate p-values, followed by a Benjamini-Hochberg correction in R to generate FDR-adjusted p-values. For FDR-adjusted p values < 0.05 peptide abundance values were unit normalized and imported to Morpheus (Broad Institute) for display on heatmaps. When possible, protein abundance values from the whole cell lysate experiments were log2 transformed, median normalized and were subtracted from the corresponding peptide normalized values for each respective sample to correct for changes in total protein abundance.

2.15. Methyl false discovery estimation

The “Decoy PSMs” export from Proteome Discoverer 2.2 was filtered for decoy methyl PSMs and the decoy q-values from the Percolator node were extracted and compared with the target methyl PSM q-values. Target methyl PSMs were removed until a 1% FDR was achieved as described [52].

2.16. Neutral loss identification in MaxQuant

The modifications SDMA and ADMA were added to MaxQuant’s library with the added mass of dimethyl on arginine and the corresponding neutral loss masses of 31.042 for SDMA and 45.058 for ADMA assigned in the “Neutral Loss” Table in Configuration [28]. The missed cleavage rate was set to 5 and all other settings were kept unchanged. All RAW files were searched with monomethyl(K/R), ADMA, SDMA, and oxidation of methionine as variable modifications. Carbamidomethylation was kept as a fixed modification. Neutral losses and their masses were extracted from the msms.txt file. Only

target methyl peptides that passed the 1% Methyl FDR filter were considered for analysis. An Andromeda cutoff score of 56 was also used to filter spectra to reduce the number of incorrect assignments. A custom R script was used to remove neutral losses that did not have the corresponding b/y ion present (example: if y6* but not y6 was present, the neutral loss was removed). A few spectra were confirmed by manual inspection to ensure the accuracy of the Andromeda search. For identified ADMA/SDMA neutral losses, the Andromeda output was matched to Proteome Discoverer data by MS2 scan number.

2.17. Motif analysis

Two sample motif analysis was performed using Two Sample Logo [53].

2.18. Protein gene ontology

Gene ontologies were performed using PantherDB with a background mouse proteome for biological process, molecular function, and cellular component ontologies.

2.19. Confocal immunofluorescence microscopy

WT and mKO EDL and SOL muscles stored in OCT were sectioned on a cryostat (Thermo Fisher Scientific, Waltham, Massachusetts, USA) into 10 μm slices. Staining of the MHC isoforms was performed as previously described [54] using primary antibodies against MHC I (BA-F8), MHC I and IIa (BF-35), and MHC IIx (6H1) (Developmental Studies Hybridoma Bank, Iowa City, Iowa, USA), followed by isotype-specific fluorescent secondary antibodies (Invitrogen, Carlsbad, California, USA). This allowed for the identification of type I (1853872, Invitrogen), Type IIa and I (1820808, Invitrogen), and type IIx (1828021, Invitrogen) fibers. All slides were viewed with the Nikon Eclipse Ti Microscope (Nikon Instruments, Mississauga, ON, Canada), equipped with a high-resolution Photometrics CoolSNAP HQ2 fluorescent camera. Images were captured and analyzed using the Nikon NIS Elements AR 3.2 software. All images were obtained with the ×20 objective. For each sample, all fibers of each specific fiber type were counted to obtain fiber percentage, while CSA was circled and measured in a maximum of 150 fibers per fiber type. Investigators performing counting were blinded to the experimental conditions.

Immunohistochemical labeling of the pre- and postsynaptic components was adapted from previous methods [55,56]. Whole EDL and SOL muscles were carefully dissected in oxygenated Ringer’s Solution (110 NaCl, 5 KCl, 1 MgCl₂, 25 NaHCO₃, 2 CaCl₂, 11 glucose, 0.3 glutamic acid, 0.4 glutamine, 5 BES (N,N-Bis(2-hydroxyethyl)-2-aminoethanesulfonic acid sodium salt, 0.036 choline chloride, and 4.34 × 10⁻⁷ cocarboxylase) and pinned in a sylgard coated 10 mm Petri Dish. Muscles were then fixed for 10 min in 4% PFA at room temperature and then permeabilized in cold methanol at –20 °C for 6 min. Nonspecific labeling was blocked by incubating muscles with 10% normal donkey serum in PBS containing 0.1% Triton X-100 for 60 min at room temperature. Motoneuron axons [chicken anti-neurofilament M, 1:2,000, Rockland Immunochemicals] and nerve terminals [mouse IgG1 anti-synaptic vesicular protein 2, 1:2,000; Developmental Studies Hybridoma Bank] were labeled overnight at 4 °C. On the following day, muscles were incubated with secondary antibodies, goat anti-mouse IgG1 Alexa-594, and donkey anti-chicken Alexa-594 (all 1:500, Jackson ImmunoResearch Laboratories) for 60 min. Postsynaptic acetylcholine receptors were labeled with Alexa-488-conjugated-α-bungarotoxin (1:500, Invitrogen) for 60 min. All antibody incubations were performed in PBS containing 0.1% Triton X-100 and 2% normal donkey serum at room temperature. After each

step, muscles were rinsed 3 times in PBS containing 0.01% Triton X-100 for 5 min. Samples were then mounted in Prolong Gold antifade reagent (Invitrogen). Images were captured with confocal microscopy (X60, 1.4 NA oil immersion; Nikon Instruments, Mississauga, Ontario, Canada).

2.20. Transmission electron microscopy (TEM)

Muscles were fixed, embedded, and cut into thin sections (70 nm) with an ultramicrotome (Ultracyte E; Reichert, Vienna, Austria). Samples were placed onto Cu/Pd grids and stained in uranyl acetate for 5 min and then in lead acetate for 2 min [57]. These analyses were completed by a skilled technician at the McMaster University Medical Center who was blinded to the experimental groups.

Muscle fragments were photographed at $\times 15,000$ magnification using electron microscopy (JEOL 1200 Ex, Japan) as well as at $\times 30,000$ and $\times 75,000$ for a zoomed in images of specific structures of interest. The $\times 15,000$ magnification allowed both subsarcolemmal and intermyofibrillar mitochondria, as well as a nucleus of the muscle cell to be visible in each image. 10 fibers were analyzed per TA muscle for a total of 80 images that were subsequently assigned for analysis to 3 independent laboratory members, who were blinded to study conditions. TEM analysis on $\times 15,000$ magnification images involved the measurement of mitochondrial size (mean area, μm^2), distribution (number per μm^2) and density ($\mu\text{m}^2 \times \text{number per } \mu\text{m}^2 \times 100$) using the software ImageJ, where mitochondria were manually outlined and converted to genuine sizing via a calibration grid. The criteria utilized to identify mitochondria included the presence of a full or partial outer membrane with visible cristae inside. Mitochondria observed to be over 20% swollen, or containing abnormal cristae (e.g., paracrystalline inclusions, cristae linearization and angular features, concentric cristae, etc.), compartmentalization, outer membrane lesions, and giant mitochondria, as previously reported [58] were labelled as abnormal and subsequently removed from size, distribution, and density analyses. Any abnormal mitochondria observed to be over 50% swollen, or with large outer membrane breaches were additionally labelled as grossly distorted.

2.21. Preparation of permeabilized fibers

The technique used to prepare the EDL and SOL muscles has previously been described [59,60]. Mice were euthanized by cervical dislocation and muscles were quickly removed. Immediately after excision, muscles were placed in ice-cold Biopsy Preservation Solution (BIOPS) buffer (50 mM K-MES, 7.23 mM K2EGTA, 2.77 mM CaK2EGTA, 20 mM imidazole, 20 mM taurine, 5.7 mM ATP, 14.3 mM phosphocreatine, and 6.56 mM MgCl₂, pH 7.1). Each muscle was trimmed of connective tissue and fat and divided into several small muscle bundles (~4–5 mg wet weight). Fiber bundles were separated with fine forceps and permeabilized in 50 $\mu\text{g}/\text{mL}$ saponin in BIOPS for 30 min at 4 °C. Bundles were also treated with 35 μM 2,4-dinitrochlorobenzene (CDNB) during the permeabilization step to deplete glutathione and allow for detectable rates of mitochondrial H₂O₂ emission. Muscle fibers were then washed in Buffer Z (105 mM K-MES, 30 mM KCl, 10 mM KH₂PO₄, 5 mM MgCl₂, 1 mM EGTA, 5 mg/mL BSA, pH 7.4) at 4 °C for at least 30 min before analysis.

2.22. Mitochondrial respiration and H₂O₂ emission

High-resolution respirometry was performed using the Oxygraph-2k system (Oroboros Instruments, Innsbruck, Austria) at 37 °C with [O₂] at ~250–400 μM . Chambers were calibrated prior to adding 2 mL of Buffer Z, blebbistatin (BLEB; 5 μM), horseradish peroxidase (4 U/mL), superoxide dismutase (30 U/mL), and Amplex Red (10 μM). Fluorometric sensor calibrations were performed by adding 0.1 μM H₂O₂

prior to all substrate addition. Pyruvate (5 mM) and malate (2 mM) were added initially, followed by ADP (5 mM), glutamate (5 mM), Cyto C (10 mM) and succinate (10 mM). H₂O₂ emission was measured simultaneously with O₂ consumption using the O₂k-Fluo LED2-Module (Oroboros Instruments, Innsbruck, Austria). Respiration and H₂O₂ emission values were normalized to wet muscle weights.

2.23. Statistical analyses

Differences between group means were evaluated using a Student's t-test, non-parametric Kolmogorov–Smirnov test, or an ANOVA as appropriate, unless otherwise stated elsewhere in the Methods. Statistical tests were performed on the raw data. Statistical differences were considered significant if $p < 0.05$. Data in graphical summaries are means \pm SEMs.

3. RESULTS

3.1. Skeletal muscle transcriptome of CARM1 mKO mice

To understand the role that CARM1 plays in the maintenance and remodelling of skeletal muscle, we generated CARM1 mKO mice (Figure 1A) [19]. We then examined in muscles from wildtype (WT) and mKO mice transcript levels of CARM1 and other key members of the PRMT family including PRMT1, -5, and -7 using quantitative reverse transcription PCR (RT-qPCR). In both the extensor digitorum longus (EDL) and soleus (SOL) muscles PRMT1, -5, and -7 mRNA levels were similar between genotypes (Figure 1B). PRMT1 transcript content was higher in the slow, oxidative SOL muscle compared to the faster, more glycolytic EDL muscle whereas PRMT5, and -7 levels were similar between EDL and SOL. CARM1 mRNA levels were similar between muscles in WT mice with residual expression in mKO animals. Following this we sought to uncover global transcriptional changes in mKO animals versus their WT littermates using RNA-seq analysis of tibialis anterior (TA) muscles. 483 differentially expressed genes (206 upregulated, 277 downregulated; false discovery rate or FDR <5%) were identified in mKO compared to WT mice (Figure 1C). Closer examination of these data revealed a distinct pattern of clustering (FDR <1% and fold change >2) between genotypes (Figure 1D). The top 10 upregulated and downregulated genes in mKO muscle with their respective log₂ ratios are listed in Table 1. Over-represented gene ontology (GO) terms in the upregulated gene set (FDR <5%) revealed a strong enrichment in several muscle-specific categories including regulation of muscle contraction, actin and tropomyosin binding, troponin complex, and metabolism (Figure 1E). The downregulated gene set revealed a muscle atrophy gene signature in mKO animals relative to WT mice (Figure 1F). Previous work has implicated CARM1 in muscle atrophy [13,15,19,24–26], thus we more closely examined our results by comparing the data to publicly available biosets relating to muscle atrophy and muscular dystrophy using the Illumina BaseSpace™ Correlation Engine [49]. A targeted meta-analysis was performed between the mKO bioset and 30 individually significant correlated biosets obtained from 10 muscle atrophy studies [61–70] and 32 Biosets obtained from 10 muscular dystrophy studies [71–80]. This meta-analysis revealed that of the 206 upregulated genes (FDR <5%) in CARM1 mKO muscle, 98, 70 and 41 were correlated with biosets of muscle atrophy, muscular dystrophy, and both of these conditions, respectively (Figure 1G). Similar analysis of the 277 downregulated genes in CARM1 mKO muscle uncovered 161, 110 and 74 correlated features with muscle atrophy, muscular dystrophy, and both cohorts, respectively (Supplementary Table 1). RT-qPCR-based validation of correlated genes identified via meta-analysis

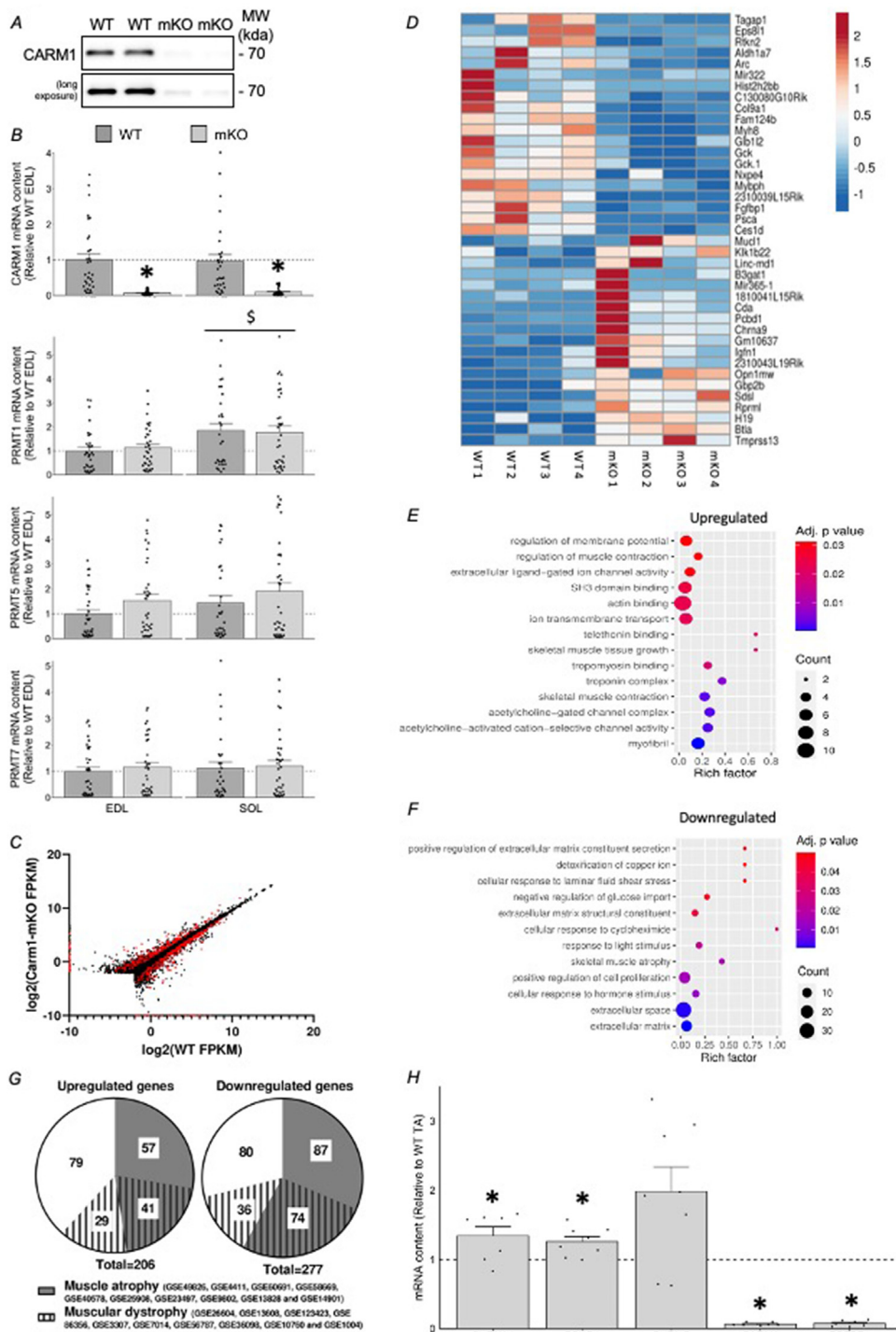


Figure 1: RNA-seq analysis of skeletal muscle from CARM1 mKO mice. (A) Representative Western blots for CARM1 (short and long exposure) in the tibialis anterior (TA) muscle from male wildtype (WT) animals and age-matched, skeletal muscle-specific CARM1 knockout (mKO) littermates. Approximate molecular weights (MWs) in kilodaltons (kda) to the right. (B) Graphical summary of CARM1, PRMT1, PRMT5, and PRMT7 transcript levels in extensor digitorum longus (EDL) and soleus (SOL) muscles. Bars indicate group means, whiskers represent SEMs, points illustrate individual results, and the dotted lines denote 1. Data are displayed relative to the WT EDL. Statistical analysis was completed using a 2-way ANOVA and Tukey's post hoc test. *, $p < 0.05$ vs. WT; \$, $p < 0.05$ vs EDL (main effect of muscle type). $n = 29-37$. (C) WT vs mKO gene fragments per kilobase of transcript per million mapped reads (FPKM) scatter plot (FDR $< 5\%$). Highlighted in red are differentially expressed genes. (D) Heat map showing differentially expressed genes with a minimum log fold change (FC) of 2.0 and $< 1\%$ false discovery rate (FDR) in TA muscle from WT and mKO littermates. $n = 4$. Bubble plots showing the distribution and size of over-represented gene ontology (GO) terms in the upregulated (E) and downregulated gene sets (F). (G) Pie charts representing commonality in upregulated and downregulated genes among the CARM1 mKO, muscle atrophy and muscular dystrophy biosets following a BaseSpace Correlation Engine meta-analysis. White portion = only altered in CARM1 mKO dataset; grey area = modified in CARM1 mKO and muscle atrophy data; striped region = changed in CARM1 mKO and muscular dystrophy data; grey striped area = commonly modified genes in all conditions. (H) Graphical summary of cholinergic receptor nicotinic alpha 1 subunit (CHRNA1), forkhead box O1 (FOXO1), cholinergic receptor nicotinic gamma subunit (CHRN3), CARM1, and fibroblast growth factor binding protein 1 (FGFBP1) mRNA levels in mKO TA muscles displayed relative to WT mice. Bars indicate group means, whiskers represent SEMs, points illustrate individual results, and the dotted lines denote 1. Statistical analysis was completed using a student's t-test. *, $p < 0.05$ vs. WT. $n = 7-8$. (For interpretation of the references to color/colour in this figure legend, the reader is referred to the Web version of this article.)

Table 1 — Top 10 up- and down-regulated genes in the skeletal muscle of CARM1 mKO mice.

	Gene	Locus	log ₂ (WT FPKM)	log ₂ (mKO FPKM)	log ₂ (Ratio)	
Upregulated	Chrna9	chr5:65967123-65977486	-3.25	2.24	5.5	
	Opn1mw	chrX:74127465-74150917	-1.09	3.33	4.42	
	Aloxe3	chr11:69126376-69149115	-5.38	-1.74	3.64	
	Gm10637	chr8:87169746-87199867	-1.71	1.63	3.34	
	Linc-md1	chr1:20669881-20684255	-1.09	1.94	3.03	
	Mir133b	chr1:20669881-20684255	-1.09	1.94	3.03	
	Igfn1	chr1:135951481-136006342	2.21	5.16	2.95	
	4930526I15Rik	chr9:124422624-124424856	-2.45	0.41	2.86	
	Cda	chr4:138336509-138367981	1.04	3.89	2.85	
	Klk1b22	chr7:44112663-44116920	1.94	4.77	2.83	
	Downregulated	Hist2h2bb	chr3:96269699-96270192	-0.89	-10	-9.11
		Psca	chr15:74714838-74717065	-1.66	-10	-8.34
		2310039L15Rik	chr10:95336275-95364925	1.56	-3.54	-5.1
		Eps811	chr7:4460707-4480487	-0.04	-4.84	-4.8
		Gm4737	chr16:46152990-46155077	-0.34	-4.72	-4.38
Fgfbp1		chr5:43978857-43981799	2.43	-1.57	-3.99	
Gck		chr11:5900739-5950081	3.82	0.35	-3.47	
Col9a1		chr1:24177609-24252738	0.5	-2.67	-3.16	
Fam124b		chr1:80186904-80229614	2.08	-0.96	-3.03	
Myh8		chr11:67277123-67308633	2.9	0.2	-2.7	

Chr, chromosome; FPKM, fragments per kilobase of transcript per million mapped reads; mKO, skeletal muscle-specific CARM1 knockout mice; WT, wildtype. $n = 4$.

was performed in TA muscles and similar to our RNA-seq data cholinergic receptor nicotinic alpha 1 subunit (CHRNA1), forkhead box O1 (FOXO1), CARM1, and fibroblast growth factor binding protein 1 (FGFBP1) transcript levels were significantly different in mKO muscle versus WT (Figure 1H). Cholinergic receptor nicotinic gamma subunit (CHRNA3) mRNA exhibited a strong statistical trend ($p = 0.055$) to be higher in mKO TA muscle.

3.2. Arginine methylome profiling of skeletal muscle

To understand the role of CARM1 in skeletal muscle arginine methylation, we first sought to define the arginine methylome in this tissue. We employed a previously optimized workflow [27] to enrich methyl peptides from mouse quadriceps (QUAD) muscles using complementary immunoaffinity purification (IAP) and high pH strong cation exchange (SCX) techniques followed by liquid chromatography-mass spectrometry (LC-MS) (Figure 2A). Analysis of muscles from WT mice identified over 1,150 methylation sites on 313 proteins with a strict 1% methyl-peptide FDR (Supplementary File 1). GO analyses revealed that methylarginine peptides were enriched for RNA binding, mRNA processing, muscle system processes, and actin filament binding (Figure 2B). Analysis of IAP and SCX data revealed that each method enhanced the expected type of arginine methylation (Figure 2C). In addition, there was little overlap of unique methyl peptides refined by IAP and SCX (Figure 2D), highlighting the importance of employing both enrichment techniques [27]. IAP and SCX generally enriched singly methylated peptides, with some IAP-enriched peptides containing up to 4 methylation sites (Figure 2E).

We also observed that 5.6% of arginine residues from arginine methylated proteins were methylated (Figure 2F). In comparison, 6.9%, 7.2%, and 12.7% of serine, threonine, and tyrosine residues, respectively, are phosphorylated [81], 10.3% of lysine residues are ubiquitinated [82], and 6.9% of arginine residues are ADP-ribosylated [83] on proteins that bear those marks in skeletal muscle (Table 2). Neutral loss analysis of WT dimethylarginine peptides showed an approximate 6:1 ratio of asymmetric dimethylarginine (ADMA) to symmetric dimethylarginine (SDMA) modifications with a small fraction of peptides bearing both modifications within the same amino acid sequence (Figure 2G). This ratio of ADMA:SDMA is consistent with

previous reports of 6:1 [27] and 10:1 [84]. Collectively, these data suggest that arginine methylation in skeletal muscle is observed with a similar prevalence to that of the much more comprehensively studied serine and threonine phosphorylation, as well as lysine methylation.

3.3. CARM1-mediated arginine methylome in skeletal muscle

Following this, we explored how the removal of CARM1 in skeletal muscle impacts the arginine methylome in this tissue. In the TA muscle we found that global monomethylarginine (MMA) marks were significantly reduced (-10%) in mKO muscle relative to WT (Figure 3A,B), however the specific unmethylated form of SmB was similar between genotypes. CARM1 mKO had no impact on PRMT1, -5, and -6 content in skeletal muscle. In contrast, PRMT7 expression was significantly upregulated (+45%) in muscles from mKO mice compared to their WT littermates. We then quantified the specific impact of CARM1 mKO on the arginine methylome in QUAD muscles of WT and CARM1 mKO animals using our comprehensive LC-MS proteomics approach. We found 16 MMA peptides that were significantly increased and 20 MMA peptides that were significantly decreased in mKO muscles (FDR-corrected p -value < 0.05) (Figure 3C,D). When possible, we normalized the abundance of methylarginine peptides to total protein levels. Notably, we were unable to normalize any upregulated MMA peptides to total protein levels, so we cannot exclude that change in total protein abundance caused the observed upregulation in these MMA sites. Motif analysis uncovered a [P/A]FVT sequence that was enriched in MMA sites decreased in CARM1 mKO muscles, whereas the MMA sites that were unchanged with CARM1 mKO were enhanced for the RGG motif commonly found in methylarginine peptides (Figure 3E). GO analysis revealed that MMA peptides that were significantly decreased in mKO animals were enriched for several muscle terms, including sarcomere organization, muscle cell development, myofibril assembly, sarcomere localization, and Z-disc localization (Figure 3F).

Next, we examined protein dimethylarginine (DMA) including both ADMA and SDMA marks. ADMA levels of bona fide CARM1 targets [8,9] BRG1-associated factor 155 (BAF155) and polyadenylate-binding protein 1 (PABP1), as well as marked CARM1 substrates were reduced by 40–65% in muscles from mKO mice relative to WT (Figure 4A,B). Global myocellular ADMA and SDMA content, which are largely

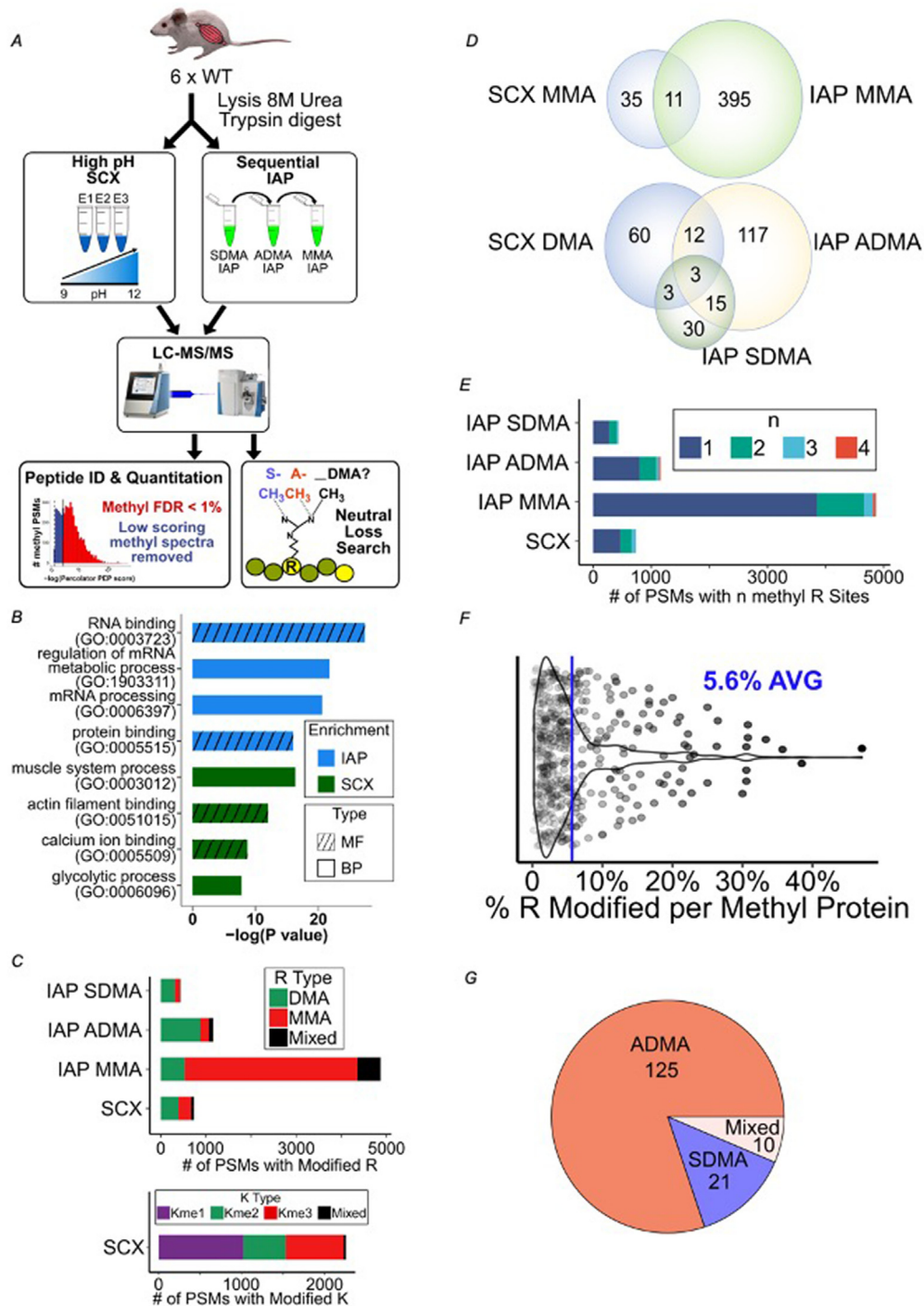


Figure 2: Arginine methylproteomic profiling of skeletal muscle. (A) Overview of methylarginine proteomic workflow. Mouse quadriceps muscles from WT animals were subject to high pH strong cation exchange (SCX) and immunoaffinity purification (IAP) to enrich for peptides containing symmetric dimethylarginine (SDMA), asymmetric dimethylarginine (ADMA), and monomethylarginine (MMA). Samples were then analyzed using liquid chromatography-mass spectrometry (LC-MS). Identified spectra were corrected to a 1% methyl FDR and annotated for neutral loss to discriminate ADMA from SDMA sites. $n = 6$. (B) GO of protein accessions from methylarginine peptides compared to the mouse background proteome, separated by enrichment method (sorted by Biological Process and Molecular Function). Ontologies passed an FDR threshold < 0.25 . (C) Peptide spectral matches (PSMs) of each methyl type are shown for each enrichment experiment. High confidence spectra passing the 1% methyl FDR were considered. Arginine methylation type is organized into dimethylarginine (DMA), MMA, or mixed. Mixed peptides contained a mixture of mono/di methylation on arginine (R) and mono/di/trimethylation on lysine (K) on the same peptide. Values shown are the sum of identified PSMs from $n = 6$ samples. (D) Overlap of identified methylarginine peptides from each enrichment method. (E) Number of PSMs with n methyl sites per spectrum. (F) Violin plot of the percent of arginine residues methylated on methylated proteins. All arginine residues from each protein were considered in the denominator even if protein coverage was not 100%. The average of all identified proteins is shown with a blue vertical line. (G) Pie chart of dimethylarginine peptides showing either ADMA, SDMA, or mixed neutral loss from WT samples. (For interpretation of the references to color/colour in this figure legend, the reader is referred to the Web version of this article.)

Table 2 — Distribution of arginine methylation sites compared to other widespread posttranslational modifications.

PTM	PTM occurrence in mouse skeletal muscle dataset	PTM occurrence in mouse (Phosphosite database)	Amino acid occurrence in mouse
Lys ubiquitination	10.3% [82]	14.5% [91]	5.65%
Ser phosphorylation	6.9% [81]	11.9% [91]	8.41%
Thr phosphorylation	7.2% [81]	8.8% [91]	5.35%
Tyr phosphorylation	12.7% [81]	13.9% [91]	2.69%
Arg methylation	5.6% (present study)	6.2% [91]	5.63%
Lys methylation	6.8% (present study)	6.2% [91]	5.65%
Arg ADP-ribosylation	9.2% [83]	—	5.63%
Lys acetylation	—	10.1% [91]	5.65%

Analysis of [82] was completed in 10-week-old male C57BL/6 mice with an unspecified muscle. [81] utilized male C57 mice that were 8–10 weeks old, and used the gastrocnemius, soleus, and plantaris muscles. [83] analyzed hindlimb skeletal muscle in 15-week-old C57BL/6 male animals. [91] examined data across a variety of tissues in mice. ADP, adenosine diphosphate; Arg, arginine; Lys, lysine; PTM, post translational modification; Ser, serine; Thr, threonine; Tyr, tyrosine.

indicative of PRMT1 and PRMT5 methyltransferase activities, respectively, were similar between WT and mKO animals. Next, using LC-MS proteomics, we identified numerous peptides with ADMA and SDMA modifications that were differentially expressed between muscles from WT and mKO mice (Figure 4C,D). As with MMA, we normalized the abundance of DMA peptides to total protein levels when possible. Specifically, 9 DMA peptides were significantly increased, and 10 were significantly decreased in CARM1 mKO muscle relative to WT (FDR-corrected p -value < 0.05) (Figure 4C). Analysis of DMA sites revealed that a [P/A]RYPLP motif was common to downregulated DMA peptides, while motifs containing an RGG sequence did not display altered methylarginine status in mKO tissues (Figure 4E). We identified several putative CARM1 substrate sites, including synaptopodin 2-like protein (also known as myopodin) R466, R476, R953, and R955, as well as titin R296, R304, R318, R1405, and R1414 (Figure 4F). Interestingly, we also observed decreased dimethylation of R294 and R296 in ADMA IAP and increased dimethylation of R337 in SDMA IAP on isoform 3 of RNA binding fox-1 homolog 1 (Rbfox1) in mKO skeletal muscle (Figure 4G). This suggests that R294/R296 are CARM1 methylation sites and that CARM1 knockout enables a Type II PRMT to dimethylate Rbfox1 R337; however, because we did not observe neutral loss ions for these dimethylation sites, we cannot definitively say that this represents a switch from ADMA to SDMA on Rbfox1. Taken together, these data demonstrate that removal of CARM1 significantly remodels the protein arginine methylome in mouse skeletal muscle.

3.4. CARM1 influences skeletal muscle fiber type composition and neuromuscular junction morphology

We sought to understand whether the numerous muscle-specific processes and functions revealed by transcriptomic and methylproteomic analyses to be directly impacted by CARM1 translated into alterations in muscle composition, morphology, and physiology in mKO animals. To this end, we first performed immunofluorescence analysis of fiber type composition of the EDL and SOL muscles of WT and mKO mice. Myosin heavy chain (MHC) based fiber typing demonstrated muscle-specific effects of CARM1, as the myofiber composition of the EDL muscle was similar between genotypes whereas MHC type I and IIa expression in the SOL were altered between WT and mKO mice (Figure 5A,B). The average myofiber cross-sectional area (CSA) for all fiber types in both the EDL and SOL muscles were similar between WT and mKO animals (Figure 5C,D). However, we observed a significant difference in CSA distribution of both the EDL and SOL muscles between genotypes. Qualitative morphological assessment of neuromuscular junctions (NMJs) uncovered several instances of postsynaptic fragmentation, axonal blebbing, and sprouting in the EDL

and SOL muscles of mKO animals not present in their WT counterparts (Figure 5E).

3.5. Skeletal muscle mitochondrial biology in CARM1 mKO mice

Since our transcriptomic and arginine methylproteomic data also suggest that pathways involved in muscle metabolism are altered in mKO mice, we next examined mitochondrial morphology and function. Quantitative analyses demonstrated that muscle mitochondrial content, area, density, and abundance of abnormal organelles (i.e., over 20% swollen, containing abnormal cristae, or small lesions in the outer membrane) were similar between WT and mKO animals (Figure 6A,B; and data not shown). However, mKO muscle contained significantly more (+125%) grossly distorted mitochondria, defined by expansive vacuolar space, collapsed cristae, and large fissures in the outer membrane, relative to their WT counterparts (Figure 6A,C). Mitochondrial respiratory function was significantly higher in SOL versus EDL muscles of WT mice, however this muscle-specific effect was absent in mKO animals (Figure 6D,E). Protein expression of subunits of mitochondrial oxidative phosphorylation (OXPHOS) complexes I–V were similar between WT and mKO mice (Figure 6F,G).

3.6. Skeletal muscle CARM1 regulates muscle function and the integrative physiology of performance

To understand how the CARM1-mediated transcriptome, arginine methylome, and alterations in cell biology affect muscle contractile function and whole animal physiology, we first investigated WT and mKO muscle force production and contraction kinetics of the gastrocnemius (GAST)/plantaris/SOL complex in situ. Functional impairments were evident in muscles of mKO compared to WT mice before, during, and after a fatigue protocol of repetitive stimulation-induced contractions (Figure 7A). Contractile kinetics were similar between genotypes (Table 3). Next, a series of in vivo tests of integrative physiology including ambulatory activity, motor function, strength, and endurance revealed significant decrements in the speed of volitional locomotion, as well as reduced force output during limb gripping tests (Figure 7B,C). Compared to WT mice, mKO animals had significantly reduced muscle mass (-5-15%) of the QUAD, TA, and triceps (TRI), and increased mass (+15%) of the SOL muscle (Figure 7D). Finally, a separate cohort of age-matched WT and mKO littermates remained sedentary (SED) or were run on a motor-driven rodent treadmill until the inability to continue exercise was determined and their muscles were collected immediately after exercise (OAE) or 3 h later (3AE). Treadmill run time was significantly lower by 30% in mKO mice versus the WT group (Figure 7E). Both genotypes displayed similarly significant augmented (+200%) levels of

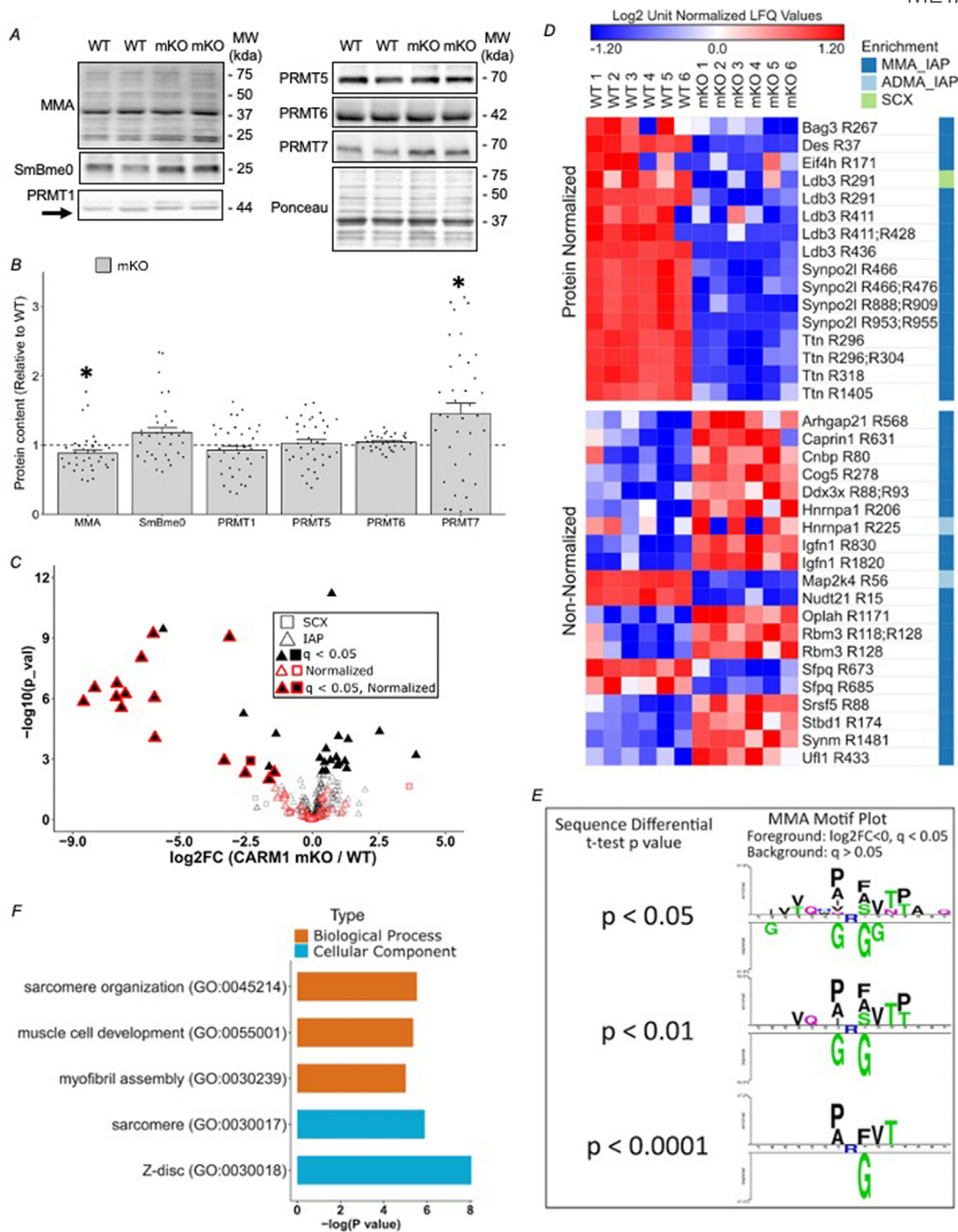


Figure 3: Monomethyl arginine analysis of CARM1 mKO muscle. (A) Representative Western blots for MMA, unmethylated form of SmB (SmBme0), PRMT1, PRMT5, PRMT6, and PRMT7 in the TA muscles from WT and mKO mice. The ponceau stain demonstrates equal loading while approximate MWs are to the right of each image. (B) Graphical summary of MMA, SmBme0, PRMT1, PRMT5, PRMT6, and PRMT7 protein levels in mKO relative to WT mice. Bars indicate group means, whiskers represent SEMs, points illustrate individual results, and the dotted line denotes 1 (or WT level). Statistical analysis was completed using a student's t-test. *, $p < 0.05$ vs. WT. $n = 29-37$. (C) Volcano plot of MMA sites comparing CARM1 mKO to WT. Sites enriched by IAP and SCX are represented by triangles and squares, respectively. Sites with an FDR-corrected p-value < 0.05 are filled in black. Sites that are normalized to the protein level are outlined in red. (D) Heatmap of MMA peptide level differences from methyl sites passing an FDR-corrected p-value < 0.05 . The enrichment technique for each site is shown in a color column on the right. $n = 6$ for each genotype. (E) Motif enrichment analysis of MMA sites downregulated in CARM1 mKO muscle. Downregulated MMA sites (\log_2 fold change [\log_2FC] < 0 and $q < 0.05$) were compared against un-changing MMA sites (FDR-corrected p-value > 0.05) using TwoSampleLogo. Enriched amino acids appear in the upper row and de-enriched amino acids appear in the lower row. The changes to the motifs as the p-value cutoff is increased is shown. (F) GO analysis of downregulated MMA protein accessions compared to mouse proteome. Displayed ontologies pass an FDR threshold of FDR-corrected p-value < 0.25 . BP = biological process, CC = Cellular Component. (For interpretation of the references to color/colour in this figure legend, the reader is referred to the Web version of this article.)

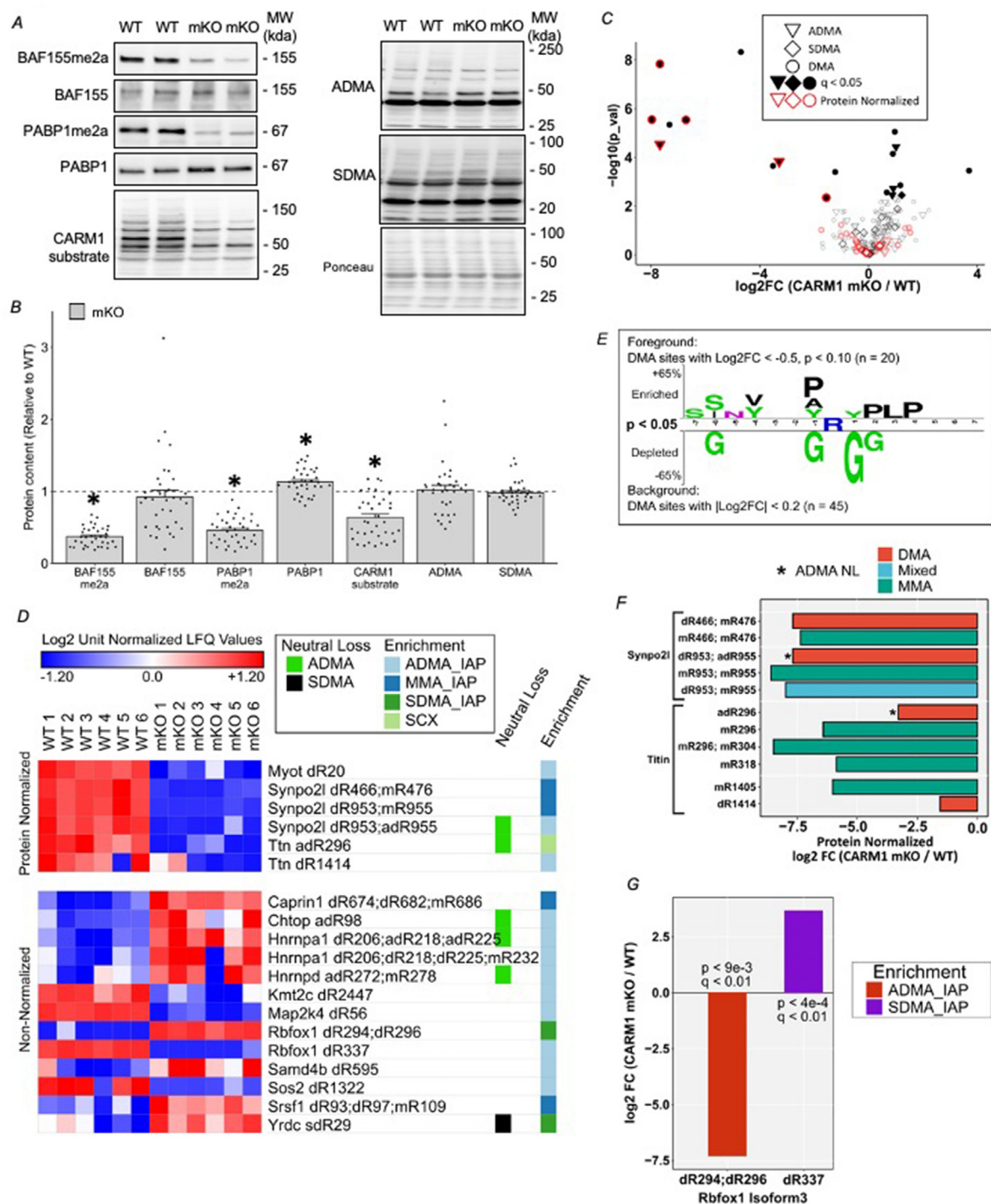


Figure 4: Quantitative and integrated analysis of CARM1-mediated protein arginine dimethylation in skeletal muscle. (A) Representative Western blots of BAF155 arginine asymmetric dimethylation (BAF155me2a), total BAF155, arginine asymmetric dimethylation of PABP1 (PABP1me2a), total PABP1, arginine methylated CARM1 substrates, ADMA at glycine and arginine-rich motifs (ADMA), and SDMA in TA muscles from WT and mKO mice. The ponceau stain demonstrates equal loading while approximate MWs (kda) are to the right of each image. (B) Graphical summary of BAF155me2a, BAF155, PABP1me2a, PABP1, CARM1 substrates, ADMA, and SDMA protein levels in the TA muscles of mKO mice relative to WT animals. Bars indicate group means, whiskers represent SEMs, points illustrate individual results, and the dotted line denotes 1 (or WT level). Statistical analysis was completed using a student's t-test. *, $p < 0.05$ vs. WT. $n = 29-37$. (C) Volcano plot of dimethylarginine sites showing neutral loss, \log_2 fold change, and whether the site was normalized to the protein level. Different shapes denote ADMA, SDMA, or DMA. Sites with an FDR-corrected p -value < 0.05 are filled in black. Sites that are normalized to the protein level are outlined in red. (D) Heatmap of significantly altered (FDR-corrected p -value < 0.05) protein normalized dimethylation sites and non-protein normalized dimethylation sites. Raw LFQ values were normalized to their respective protein level if available. The prefixes [d] and [m] denote the type of methylation, di- or mono-respectively, and neutral losses are indicated with an asterisk and either [ad] or [sd] for asymmetric or symmetric neutral loss, respectively. The enrichment technique for each site is shown in a color column on the right. $n = 6$ for each genotype. (E) Two sample motif plot with foreground of dimethylation sites with $\log_2FC < -0.5$ and $p < 0.1$ compared to background motifs that are unchanging $|\log_2FC| < 0.2$. (F) Integrated analysis of significant (FDR-corrected p -value < 0.05) putative substrates of CARM1 showing decrease in mono and dimethylation in CARM1 mKO. Neutral loss is denoted with an asterisk. Mixed peptides contained a mixture of mono/di methylation on R sites. (G) Potential ADMA to SDMA methyl switching of isoform 3 of Rbfox1 sites identified in ADMA and SDMA IAPs. (For interpretation of the references to color/color in this figure legend, the reader is referred to the Web version of this article.)

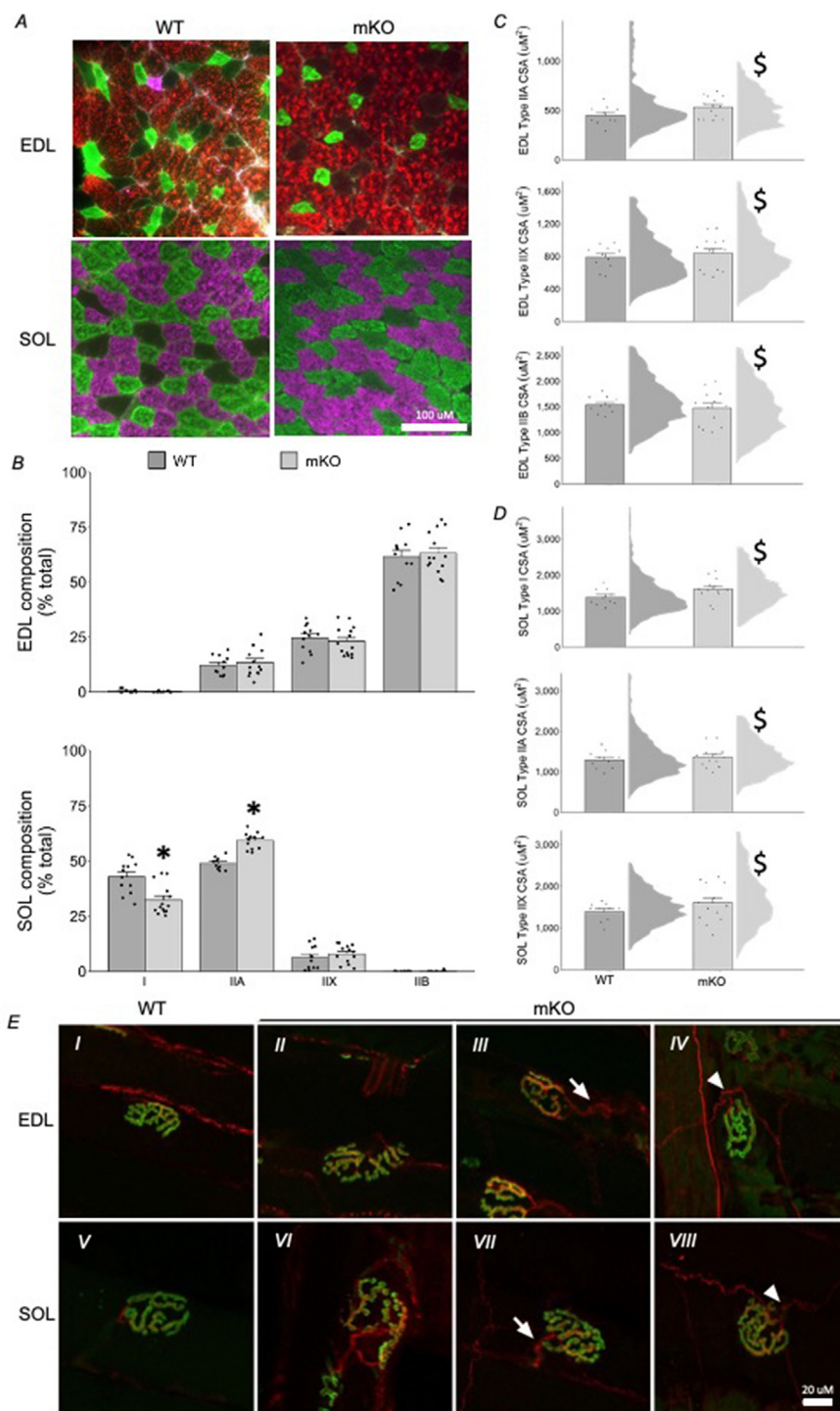


Figure 5: Myofiber phenotypes differ between WT and mKO mice. (A) Representative immunofluorescence images of myosin heavy chain (MHC) type I (pink), IIa/I (green), IIx (black), and IIb (red) in EDL and SOL muscles of WT and mKO littermates. (B) Graphical summaries of EDL (top) and SOL (bottom) myofiber MHC composition in both genotypes. (C) Graphical summaries with raincloud plots showing the average cross-sectional area (CSA) (bars) and data distribution (clouds) of each fiber type in the EDL (C) and SOL (D) muscles of WT and mKO mice (μM^2). Bars are indicative of group means, whiskers denote SEMs, and points represent individual data while clouds show data distribution. A 2-way ANOVA with Tukey's post hoc test was used to compare data in (B), while a student's t-test was used to compare average CSA for each fiber type and a non-parametric KS test was used to analyse data distribution in (C-D). *, $p < 0.05$ vs. WT (ANOVA); \$, $p < 0.05$ vs. WT (KS test). Scale bars = 100 μM $n = 11-14$. (E) Typical confocal immunofluorescence images of the neuromuscular junction in the EDL and SOL muscles of WT (panels I and V) and mKO animals (panels II-IV, VI-VIII). Neurofilament M and synaptic vesicle 2 (red) stains denote the presynaptic architecture of the NMJ, while α -bungarotoxin (green) marks postsynaptic acetylcholine receptors. Postsynaptic fragmentation was observed in the EDL (III) and SOL (VI) muscles of mKO animals. Axonal blebbing (arrows in panels III and VII) and sprouting (arrowheads in panels IV and VIII) were also observed in the EDL and SOL muscles of mKO animals. (For interpretation of the references to color/colour in this figure legend, the reader is referred to the Web version of this article.)

phosphorylated AMPK (pAMPK) in the TA muscles of animals in the OAE group compared to SED mice (Figure 7F,G). Total AMPK content was modestly, but significantly increased in mKO muscles relative to WT (Figure 7F,H). AMPK activation status (i.e., the ratio of the active, phosphorylated form of the enzyme relative to the total content of the protein) was significantly elevated (+220% in WT, +185% in mKO) in the OAE group versus SED, and then returned to basal levels at 3AE in both genotypes (Figure 7I). PGC-1 α protein content was not altered by exercise, but a significant main effect of genotype was observed (Figure 7F,J). Both the EDL and SOL muscles from WT animals displayed significantly increased mRNA levels of exercise-induced PGC-1 α (Figure 7K,L). In contrast, no increase in PGC-1 α transcripts were observed following acute exercise in mKO animals.

4. DISCUSSION

In the present study, we attempted to advance understanding of CARM1 biology in skeletal muscle. We found that the occurrence of arginine methylation in skeletal muscle *in vivo* is comparable to phosphorylation and ubiquitination, which confirms and extends earlier findings in other cell types [85]. Moreover, skeletal muscle-specific removal of CARM1 markedly remodeled transcriptomic and proteomic signatures with gene ontology analyses revealing several critical cell processes impacted in muscles of mKO mice, including muscle contraction and atrophy. We then validated these findings using a series of complementary molecular and functional assays of muscle biology and integrative physiology, which confirmed the omic profiles by demonstrating altered skeletal muscle contractile and NMJ characteristics, as well as decreased ability to exercise in CARM1 mKO animals as compared to their WT littermates. The diminished exercise capacity in mKO mice was accompanied by attenuated exercise-induced gene expression of the master regulator of neuromuscular plasticity PGC-1 α despite a preservation of upstream AMPK phosphorylation, which suggests that CARM1 regulates AMPK-PGC-1 α activity during conditions of muscle plasticity, corroborating and expanding on recent reports [19]. Taken together, our findings assert an elevated prominence of arginine methylation in skeletal muscle, particularly that regulated by CARM1, as well as reveal the necessity for the methyltransferase to maintain and remodel muscle homeostasis.

Protein arginine methylation is a critical modification in health and disease [2,5], and several recent, elegant studies have surveyed arginine methylation in various cell types, including HEK293 and numerous cancer models [27–31,86,87]. However, the impact of this mark in skeletal muscle remains largely undefined. By utilizing a sophisticated methodological approach that combines 2 orthogonal methyl peptide enrichment techniques [27], we identified over 1,150 arginine methylation sites on 313 proteins in skeletal muscle. The high number of arginine methylation sites found in our data, as well as their role in critical cell functions such as mRNA processing, RNA and protein binding, as well as general muscle system processes, highlight for the first time the importance of this posttranslational modification in skeletal muscle. Indeed, closer examination of our results uncovered levels of arginine methylation in muscle to be 5.6%, while serine and threonine phosphorylation and lysine ubiquitination, which are alternative posttranslational modifications highly characterized for their ability to regulate skeletal muscle phenotype maintenance and plasticity [12,88–90], were 7–10% [81–83,91]. Thus, the current study further supports a relationship between arginine methylation and other posttranslational modification sites [85,92,93]. With recent advances in proteomic technologies, functional crosstalk between protein

modifications has emerged [94–96], therefore additional work will examine the role that arginine methylation plays in this phenomenon within skeletal muscle.

Using bioinformatic tools, we scanned preferred motif sequences to predict PRMT substrates in skeletal muscle [97,98]. Contrary to PRMT1 and PRMT5 which prefer arginine- and glycine-rich RGG/RG sequences, earlier work indicated that CARM1 targets arginine residues neighboring PGM motifs [1,5,99,100]. However, while more recent research has confirmed the enrichment of proline, a high prevalence of glycine or methionine residues in CARM1 recognition sequences was not validated [31,101,102]. Similarly, in the current study, MMA sites that decreased in CARM1 mKO muscles were enriched for a [P/A]RFVT sequence, while a [P/A]RYPLP motif was common to downregulated dimethylarginine-marked peptides. In both instances, motifs containing an RGG sequence did not display altered methylarginine status in mKO tissues, which suggests that CARM1 removal impacts methylation specifically at proline rich motifs. Therefore, like other cell types surveyed, CARM1 in skeletal muscle has distinct substrate targeting when compared to other members of the PRMT family. This corroborates a preference for CARM1 methylation at proline-enriched motifs, which may aid in predicting potential CARM1 methylation sites affecting muscle biology in health and disease.

Bioinformatic analyses of our transcriptomic and arginine methyl-proteomic data indicated that muscle contraction and NMJ biology were significantly altered in CARM1 mKO animals versus their WT counterparts. To both confirm and expand on these results, we examined several cellular and molecular outcomes of muscle biology, as well as metrics of performance and integrative physiology. To this end, first we observed in mKO mice a muscle-specific remodelling of MHC isoforms, the primary molecular motor of contractile machinery. This occurred coincident with a broad shift in CSA distribution in all fiber types in both fast, glycolytic, and slower, more oxidative muscles. Similar muscle phenotype changes have previously been observed in a variety of muscle disorders [103]. Interestingly, synthesis of our transcriptomic results with publicly available datasets showed a total of 115 genes that were positively correlated, either up- or downregulated, between CARM1 mKO and muscle atrophy and dystrophy conditions. Taken together, these results suggest that CARM1 mKO mice display a muscle disease phenotype and further highlight the importance of CARM1 in the regulation of muscle atrophy [15,19,24,25]. Future work exploring how this mKO myopathy impacts satellite cell homeostasis during rest, repair, and regeneration would increase our understanding of the role CARM1 plays in muscle progenitor cell biology [22,23]. Next, confocal microscopy analyses of NMJ morphology in EDL and SOL muscles revealed the prevalence in mKO mice of postsynaptic fragmentation, as well as axon blebbing and sprouting that is consistent with a retrograde signal across the NMJ [104]. These structural alterations at the motor endplate also imply neurophysiological decrements [105–107], which may explain, at least in part, the attenuated force output and exercise tolerance in mKO animals. It is reasonable to speculate that the elevated fatigue in mKO animals apparent during the integrative physiological profiling is due, in part, to altered muscle contraction and NMJ morphology, as well as potentially other factors not examined here such as ATP synthesis, transport, and utilization [108]. Closer examination of key molecules involved in these processes that were alternatively methyl marked in mKO mice, including titin [109], Rbfox1 [110], and 5-oxoprolinase, ATP-hydrolysing [111,112], is warranted to fully elucidate the molecular mechanisms that are responsible for the functional decrements in mKO mice. Finally, we sought to examine how CARM1 impacts molecular mechanisms of muscle plasticity in response to acute exercise. When

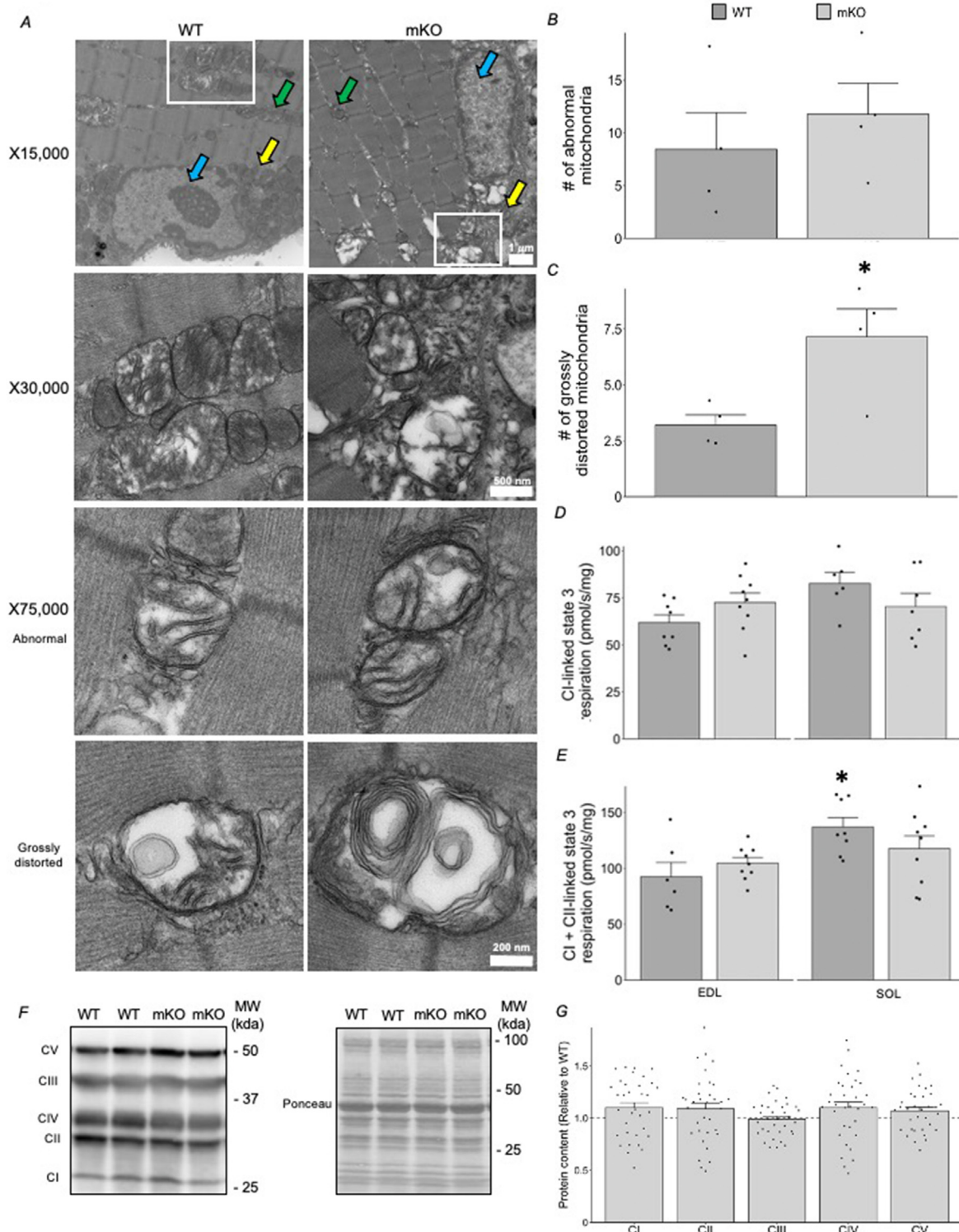


Figure 6: *Dysmorphic mitochondria in CARM1 mKO animals.* A) Representative transmission electron micrographs of TA muscles from WT and mKO mice with X15,000 zoom (top row), X30,000 zoom (second row), and X75,000 zoom (rows 3 and 4). The third row displays abnormal mitochondria, while the fourth row depicts grossly distorted mitochondria. Blue arrow, nucleus; yellow arrow, subsarcolemmal mitochondria; green arrow, intermyofibrillar mitochondria; white box, specific area in the X15,000 image that corresponds to X30,000 image. Graphical summary of (B) all abnormal mitochondria and (C) grossly distorted mitochondria. Bars indicate group means, whiskers indicate SEMs, while points illustrate individual results. A student's t-test was used for statistical analysis. *, $p < 0.05$ vs. WT. $n = 4$. Graphical summaries of (D) mitochondrial complex (C) I-linked state 3 respiration and (E) CI + CII-linked state 3 respiration (pmol/sec/mg). Bars indicate group means, whiskers indicate SEMs, while points illustrate individual results. A 2-way ANOVA was used for statistical analysis. *, $p < 0.05$ vs. WT EDL. $n = 6-9$. (F) Typical Western blots of representative subunits of mitochondrial oxidative phosphorylation CI-CV in TA muscles from WT and mKO mice. The ponceau stain demonstrates equal loading while approximate MWs (kda) are to the right of each image. (G) Graphical summary of CI, CII, CIII, CIV, and CV protein levels in the TA muscles of mKO mice relative to WT animals. Bars indicate group means, whiskers represent SEMs, points illustrate individual results, and the dotted line denotes 1 (or WT level). Statistical analysis was completed using a student's t-test. *, $p < 0.05$ vs. WT. $n = 29-34$.

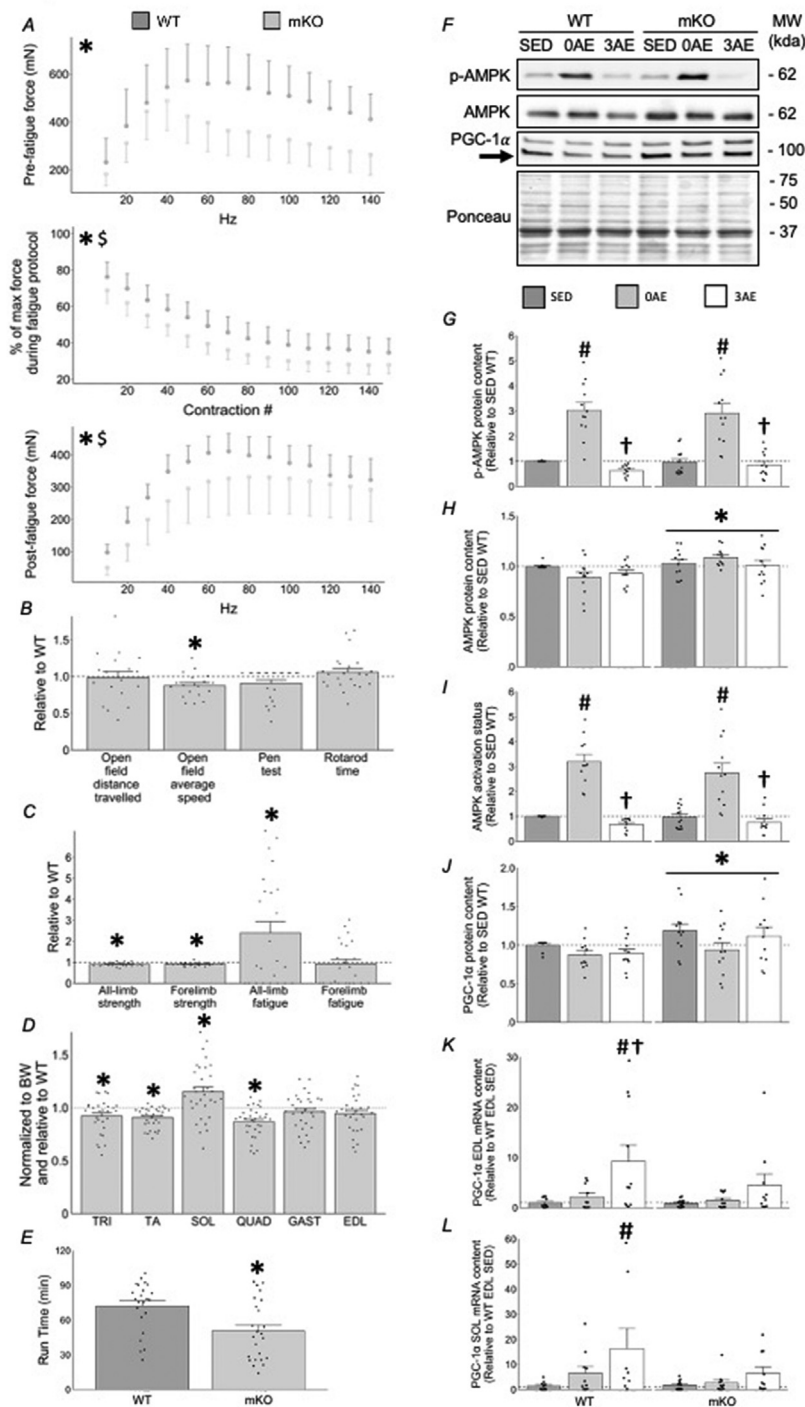


Figure 7: *CARM1* is required for maintenance of skeletal muscle function. **A**) In situ assessment of force production in the gastrocnemius/plantaris/soleus muscle complex with graphical summaries of the force–frequency relationship (top), fatigue during repetitive stimulation (middle), and force–frequency curve following fatiguing muscle stimulation protocol (bottom). Statistical analysis was completed using a 2-way ANOVA and Tukey's post hoc test. *, $p < 0.05$ vs. WT (main effect), \$, main effect of x axis. $n = 4$. Graphical summaries of functional tests classified as **(B)** movement, balance, and coordination measures, **(C)** strength and fatigue measurements, and **(D)** muscle mass relative to body mass. All data was normalized to WT animals. **(E)** Graphical summary of maximum treadmill run time. Bars indicate group means, whiskers indicate SEMs, while points illustrate individual results. A student's t-test was used for statistical analysis. *, $p < 0.05$ vs. WT. $n = 13–32$. **(F)** Representative Western blots for phosphorylated adenosine 5' monophosphate-activated protein kinase (p-AMPK), total AMPK, and peroxisome proliferator-activated receptor γ coactivator-1 α (PGC-1 α) in TA muscles from WT and mKO mice that were sedentary (SED), or immediately after exercise (OAE), or 3 h after exercise (3AE). The ponceau stain demonstrates equal loading while approximate MWs are to the right of each image. Graphical summaries of **(G)** p-AMPK, **(H)** AMPK, **(I)** AMPK activation status, calculated as the level of p-AMPK relative to AMPK content, and **(J)** PGC-1 α protein content, as well as PGC-1 α transcript levels in the EDL (**K**) and SOL (**L**). Data are displayed relative to WT SED mice. Bars indicate group means, whiskers represent SEMs, points illustrate individual results, and the dotted line denotes 1. Data was analyzed using a 2-way ANOVA and Tukey's post hoc test. #, $p < 0.05$ vs same genotype SED; †, $p < 0.05$ vs same genotype OAE; *, $p < 0.05$ vs WT (main effect of genotype). $n = 8–13$.

Table 3 — Skeletal muscle contractile kinetics in WT and mKO mice.

	Maximum twitch force (mN)	Maximum twitch force/muscle weight	Maximum tetanic force (mN)	Maximum tetanic force/muscle weight	Time to peak twitch tension (sec)	Half relaxation time (sec)	Maximum rate of force production (mN/sec)	Maximum rate of relaxation (mN/sec)
WT	122.1 ± 41.2	690.3 ± 190.9	535.2 ± 115.1	3281 ± 808.8	5.5x10 ⁻² ± 5.7x10 ⁻³	2.2x10 ⁻² ± 1.4x10 ⁻³	7018 ± 1283	5325 ± 874.8
mKO	97.8 ± 30.8	689.2 ± 241.3	334.1 ± 105.6	2362 ± 831.7	7.4x10 ⁻² ± 2.0x10 ⁻²	2.3x10 ⁻² ± 1.4x10 ⁻³	4668 ± 1468	2786 ± 881.7

Values are reported as mean ± SEM. Statistical analysis was completed using a student's t-test. $n = 4$.

challenged with the same relative exercise intensity, mKO mice demonstrated significantly lower absolute exercise capacity as compared to their healthy littermates. We observed a divergence between genotypes with respect to exercise-induced signaling, such that AMPK phosphorylation was induced in WT and mKO animals, while PGC-1 α gene expression was only elevated post-exercise in WT mice. This blunted PGC-1 α transcription detected in the mKO group may be indicative of a functional limitation in AMPK [113–115]. This is supported by recent work from our laboratory demonstrating: 1) CARM1-AMPK-specific interaction and activity in skeletal muscle, and 2) acute administration of a pharmacological AMPK activator elicited mitigated signalling and gene expression downstream of the kinase in CARM1 mKO mice compared to their WT counterparts [19]. Thus, it is reasonable to suspect that abnormal exercise-induced AMPK and PGC-1 α could translate into an attenuated adaptive potential in mKO animals, for example after a period of chronic exercise training. An alternative interpretation of the data is that since skeletal muscle PGC-1 α protein content is already significantly higher in mKO compared to WT, as we demonstrated here and earlier [19], even a robust exercise stimulus is not sufficient to further increase its expression and activity. This idea is consistent with other conditions characterized by elevated muscle PGC-1 α that are resistant to extended remodelling [116–118]. Nevertheless, data from the present study demonstrate that CARM1 is necessary for exercise-induced PGC-1 α expression, and our results here support previous work [6,19,25,119–121] that strongly suggest that the methyltransferase works with AMPK to regulate the adaptive potential of skeletal muscle.

5. CONCLUSIONS

In conclusion, this study reveals transcriptomic, methylproteomic, molecular, functional, and integrative physiological impacts of CARM1 in skeletal muscle. Notably, we observed that CARM1 regulates AMPK-PGC-1 α during acute conditions of activity-induced muscle plasticity, confirming and extending earlier work [19]. Furthermore, the data highlight a prevalence of arginine methylation in skeletal muscle that is on par with other essential posttranslational modifications, such as phosphorylation and ubiquitination. Collectively, our work establishes arginine methylation as a major mark in skeletal muscle that deserves further awareness and understanding, and additionally supports the emergence of CARM1 as a compelling player in the determination, maintenance, and remodelling of skeletal muscle biology.

6. SUMMARY

The arginine methyltransferase CARM1 regulates skeletal muscle maintenance and plasticity.

FUNDING

This work was funded by the Natural Sciences and Engineering Research Council of Canada (NSERC), the Canada Research Chairs

program, and the Ontario Ministry of Economic Development, Job Creation and Trade (MEDJCT). T.L.v., D.W.S., and S.Y.N. are NSERC scholars. E.K.W. is an Interdisciplinary Fellow of the Canadian Frailty Network. A.I.M. is an Ontario Graduate Scholarship recipient. G.V. is an associate scholar funded by the Canada (NSERC)-CREATE program (MATRIX) (RGPIN 2018–06838). V.L. is the Canada Research Chair (Tier 2) in Neuromuscular Plasticity in Health and Disease and is a MEDJCT Early Researcher.

AUTHOR CONTRIBUTIONS

Conceptualization, T.L.v. and V.L. Methodology, T.L.v., D.W.S., V.L. Formal Analysis, T.L.v., N.G.H., G.V., S.Y.N., I.A.R., E.K.W. A.I.M. Investigation, T.L.v., N.G.H., G.V., S.Y.N., E.K.W., I.A.R. Writing — Original Draft, T.L.v. and V.L. Writing — Review and Editing, T.L.v., D.W.S., N.G.H., G.V., S.Y.N., E.K.W., I.A.R., A.I.M., N.A.G., K.J.M., T.J.H., V.L. Project Administration, T.L.v. and V.L. Funding Acquisition, V.L.

DATA AVAILABILITY

Data will be made available on request.

ACKNOWLEDGMENTS

We thank Dr. Mark Bedford (MD Anderson Cancer Center, University of Texas) for the gifts of the CARM1 substrate reagent and CARM1 floxed mice. We also thank Dr. Lawrence Kazak (McGill University, Canada) for assistance with genotyping. We are grateful to the members of the Integrative Neuromuscular Biology Laboratory and to colleagues in the Exercise Metabolism Research Group at McMaster University for helpful advice and discussion.

CONFLICT OF INTEREST

None declared.

APPENDIX A. SUPPLEMENTARY DATA

Supplementary data to this article can be found online at <https://doi.org/10.1016/j.molmet.2022.101555>.

REFERENCES

- [1] Yang, Y., Bedford, M.T., 2013. Protein arginine methyltransferases and cancer. *Nature Reviews Cancer* 13(1):37–50.
- [2] Guccione, E., Richard, S., 2019. The regulation, functions and clinical relevance of arginine methylation. *Nature Reviews Molecular Cell Biology* 20(10):642–657.
- [3] Suresh, S., Huard, S., Dubois, T., 2021. CARM1/PRMT4: making its mark beyond its function as a transcriptional coactivator. *Trends in Cell Biology*.
- [4] Xu, J., Richard, S., 2021. Cellular pathways influenced by protein arginine methylation: implications for cancer. *Molecular Cell*.

- [5] Blanc, R.S., Richard, S., 2017. Arginine methylation: the coming of age. *Molecular Cell* 65(1):8–24.
- [6] Li, C., Yu, L., Xue, H., Yang, Z., Yin, Y., Zhang, B., et al., 2017. Nuclear AMPK regulated CARM1 stabilization impacts autophagy in aged heart. *Biochemical and Biophysical Research Communications* 486(2):398–405.
- [7] vanLieshout, T.L., Ljubcic, V., 2019. The emergence of protein arginine methyltransferases in skeletal muscle and metabolic disease. *American Journal of Physiology. Endocrinology and Metabolism* 317(6):E1070–E1080.
- [8] Drew, A.E., Moradei, O., Jacques, S.L., Rioux, N., Boriack-Sjodin, A.P., Allain, C., et al., 2017. Identification of a CARM1 inhibitor with potent in vitro and in vivo activity in preclinical models of multiple myeloma. *Scientific Reports* 7(1):17993.
- [9] Greenblatt, S.M., Man, N., Hamard, P.J., Asai, T., Karl, D., Martinez, C., et al., 2018. CARM1 is essential for myeloid leukemogenesis but dispensable for normal hematopoiesis. *Cancer Cell* 33(6):1111–1127 e1115.
- [10] Kumar, S., Zeng, Z., Bagati, A., Tay, R.E., Sanz, L.A., Hartono, S.R., et al., 2021. CARM1 inhibition enables immunotherapy of resistant tumors by dual action on tumor cells and T cells. *Cancer Discov.*
- [11] Wu, Q., Schapira, M., Arrowsmith, C.H., Barysyt-Lovejoy, D., 2021. Protein arginine methylation: from enigmatic functions to therapeutic targeting. *Nature Reviews Drug Discovery* 20(7):509–530.
- [12] Egan, B., Zierath, J.R., 2013. Exercise metabolism and the molecular regulation of skeletal muscle adaptation. *Cell Metabolism* 17(2):162–184.
- [13] Ljubcic, V., Khogali, S., Renaud, J.M., Jasmin, B.J., 2012. Chronic AMPK stimulation attenuates adaptive signaling in dystrophic skeletal muscle. *American Journal of Physiology - Cell Physiology* 302(1):C110–C121.
- [14] Stouth, D.W., vanLieshout, T.L., Shen, N.Y., Ljubcic, V., 2017. Regulation of skeletal muscle plasticity by protein arginine methyltransferases and their potential roles in neuromuscular disorders. *Frontiers in Physiology* 8:870.
- [15] Stouth, D.W., Manta, A., Ljubcic, V., 2018. Protein arginine methyltransferase expression, localization, and activity during disuse-induced skeletal muscle plasticity. *American Journal of Physiology - Cell Physiology* 314(2):C177–C190.
- [16] Shen, N.Y., Ng, S.Y., Toepp, S.L., Ljubcic, V., 2018. Protein arginine methyltransferase expression and activity during myogenesis. *Bioscience Reports* 38(1).
- [17] vanLieshout, T.L., Stouth, D.W., Tajik, T., Ljubcic, V., 2018. Exercise-induced protein arginine methyltransferase expression in skeletal muscle. *Medicine & Science in Sports & Exercise* 50(3):447–457.
- [18] vanLieshout, T.L., Bonafiglia, J.T., Gurd, B.J., Ljubcic, V., 2019. Protein arginine methyltransferase biology in humans during acute and chronic skeletal muscle plasticity. *Journal of Applied Physiology*.
- [19] Stouth, D.W., vanLieshout, T.L., Ng, S.Y., Webb, E.K., Manta, A., Moll, Z., et al., 2020. CARM1 regulates AMPK signaling in skeletal muscle. *iScience* 23(11):101755.
- [20] Chen, S.L., Loffler, K.A., Chen, D., Stallcup, M.R., Muscat, G.E., 2002. The coactivator-associated arginine methyltransferase is necessary for muscle differentiation: CARM1 coactivates myocyte enhancer factor-2. *Journal of Biological Chemistry* 277(6):4324–4333.
- [21] Wang, S.C., Dowhan, D.H., Eriksson, N.A., Muscat, G.E., 2012. CARM1/PRMT4 is necessary for the glycogen gene expression programme in skeletal muscle cells. *Biochemical Journal* 444(2):323–331.
- [22] Kawabe, Y., Wang, Y.X., McKinnell, I.W., Bedford, M.T., Rudnicki, M.A., 2012. Carm1 regulates Pax7 transcriptional activity through MLL1/2 recruitment during asymmetric satellite stem cell divisions. *Cell Stem Cell* 11(3):333–345.
- [23] Chang, N.C., Sincennes, M.C., Chevalier, F.P., Brun, C.E., Lalaria, M., Segales, J., et al., 2018. The dystrophin glycoprotein complex regulates the epigenetic activation of muscle stem cell commitment. *Cell Stem Cell* 22(5):755–768 e756.
- [24] Liu, Y., Li, J., Shang, Y., Guo, Y., Li, Z., 2019. CARM1 contributes to skeletal muscle wasting by mediating FoxO3 activity and promoting myofiber autophagy. *Experimental Cell Research* 374:198–209.
- [25] Hu, R., Wang, M.Q., Liu, L.Y., You, H.Y., Wu, X.H., Liu, Y.Y., et al., 2020. Calycosin inhibited autophagy and oxidative stress in chronic kidney disease skeletal muscle atrophy by regulating AMPK/SKP2/CARM1 signalling pathway. *Journal of Cellular and Molecular Medicine*.
- [26] Cheng, D., Gao, G., Di Lorenzo, A., Jayne, S., Hottiger, M.O., Richard, S., et al., 2020. Genetic evidence for partial redundancy between the arginine methyltransferases CARM1 and PRMT6. *Journal of Biological Chemistry*.
- [27] Hartel, N.G., Chew, B., Qin, J., Xu, J., Graham, N.A., 2019. Deep protein methylation profiling by combined chemical and immunoaffinity approaches reveals novel PRMT1 targets. *Molecular & Cellular Proteomics* 18(11):2149–2164.
- [28] Musiani, D., Bok, J., Massignani, E., Wu, L., Tagaglio, T., Ippolito, M.R., et al., 2019. Proteomics profiling of arginine methylation defines PRMT5 substrate specificity. *Science Signaling* 12.
- [29] Radziszewska, A., Shliaha, P.V., Grinev, V., Lorenzini, E., Kovalchuk, S., Shlyueva, D., et al., 2019. PRMT5 methylome profiling uncovers a direct link to splicing regulation in acute myeloid leukemia. *Nature Structural & Molecular Biology* 26(11):999–1012.
- [30] Lim, Y., Park, Y.E., Ha, S., Lee, J.E., Kim, H.C., 2020. A comprehensive analysis of symmetric arginine dimethylation in colorectal cancer tissues using immunoaffinity enrichment and mass spectrometry e1900367. *Proteomics*.
- [31] Maron, M.I., Lehman, S.M., Gayatri, S., DeAngelo, J.D., Hegde, S., Lorton, B.M., et al., 2021. Independent transcriptomic and proteomic regulation by type I and II protein arginine methyltransferases. *iScience* 24(9):102971.
- [32] Yadav, N., Lee, J., Kim, J., Shen, J., Hu, M.C., Aldaz, C.M., et al., 2003. Specific protein methylation defects and gene expression perturbations in coactivator-associated arginine methyltransferase 1-deficient mice. *Proceedings of the National Academy of Sciences of the United States of America* 100(11):6464–6468.
- [33] Bao, J., Di Lorenzo, A., Lin, K., Lu, Y., Zhong, Y., Sebastian, M.M., et al., 2018. Mouse models of overexpression reveal distinct oncogenic roles for different type I protein arginine methyltransferases. *Cancer Research*.
- [34] Tatem, K.S., Quinn, J.L., Phadke, A., Yu, Q., Gordish-Dressman, H., Nagaraju, K., 2014. Behavioral and locomotor measurements using an open field activity monitoring system for skeletal muscle diseases. *Journal of Visualized Experiments* 91:51785.
- [35] Liu, H., Yazdani, A., Murray, L.M., Beauvais, A., Kothary, R., 2014. The Smn-independent beneficial effects of trichostatin A on an intermediate mouse model of spinal muscular atrophy. *PLoS One* 9(7):e101225.
- [36] Aartsma-Rus, A., van Putten, M., 2014. Assessing functional performance in the mdx mouse model. *Journal of Visualized Experiments* 85.
- [37] Saleem, A., Carter, H.N., Hood, D.A., 2014. p53 is necessary for the adaptive changes in cellular milieu subsequent to an acute bout of endurance exercise. *American Journal of Physiology - Cell Physiology* 306(3):C241–C249.
- [38] Krause, M.P., Liu, Y., Vu, V., Chan, L., Xu, A., Riddell, M.C., et al., 2008. Adiponectin is expressed by skeletal muscle fibers and influences muscle phenotype and function. *American Journal of Physiology - Cell Physiology* 295(1):C203–C212.
- [39] Krause, M.P., Riddell, M.C., Gordon, C.S., Imam, S.A., Cafarelli, E., Hawke, T.J., 2009. Diabetic myopathy differs between Ins2A β +/– and streptozotocin-induced Type 1 diabetic models. *Journal of Applied Physiology* 106(5):1650–1659.
- [40] Al-Sajee, D., Nissar, A.A., Coleman, S.K., Rebalka, I.A., Chiang, A., Wathra, R., et al., 2015. Xin-deficient mice display myopathy, impaired

- contractility, attenuated muscle repair and altered satellite cell functionality. *Acta Physiologica* 214(2):248–260.
- [41] Coleman, S.K., Cao, A.W., Rebalka, I.A., Gyulay, G., Chambers, P.J., Tupling, A.R., et al., 2018. The Pleckstrin homology like domain family member, TDAG51, is temporally regulated during skeletal muscle regeneration. *Biochemical and Biophysical Research Communications* 495(1):499–505.
- [42] Romero-Calvo, I., Ocon, B., Martinez-Moya, P., Suarez, M.D., Zarzuelo, A., Martinez-Augustin, O., et al., 2010. Reversible Ponceau staining as a loading control alternative to actin in Western blots. *Analytical Biochemistry* 401(2):318–320.
- [43] Cheng, D., Vemulapalli, V., Lu, Y., Shen, J., Aoyagi, S., Fry, C.J., et al., 2018. CARM1 methylates MED12 to regulate its RNA-binding ability. *Life Science Alliance* 1(5).
- [44] Schmittgen, T.D., Livak, K.J., 2008. Analyzing real-time PCR data by the comparative CT method. *Nature Protocols* 3(6):1101–1108.
- [45] Kim, D., Pertea, G., Trapnell, C., Pimentel, H., Kelley, R., Salzberg, S.L., 2013. TopHat2: accurate alignment of transcriptomes in the presence of insertions, deletions and gene fusions. *Genome Biology* 14.
- [46] Hochberg, Y., Benjamini, Y., 1990. More powerful procedures for multiple significance testing. *Statistics in Medicine* 9:811–818.
- [47] Mi, H., Muruganujan, A., Ebert, D., Huang, X., Thomas, P.D., 2019. PANTHER version 14: more genomes, a new PANTHER GO-slim and improvements in enrichment analysis tools. *Nucleic Acids Research* 47(D1):D419–D426.
- [48] Edgar, R., Domrachev, M., Lash, A.E., 2002. Gene Expression Omnibus: NCBI gene expression and hybridization array data repository. *Nucleic Acids Research* 30(1):207–210.
- [49] Kupershmidt, I., Su, Q.J., Grewal, A., Sundaresh, S., Halperin, I., Flynn, J., et al., 2010. Ontology-based meta-analysis of global collections of high-throughput public data. *PLoS One* 5(9).
- [50] Wang, K., Dong, M., Mao, J., Wang, Y., Jin, Y., Ye, M., et al., 2016. Antibody-free approach for the global analysis of protein methylation. *Analytical Chemistry* 88(23):11319–11327.
- [51] Perez-Riverol, Y., Csordas, A., Bai, J., Bernal-Llinares, M., Hewapathirana, S., Kundu, D.J., et al., 2019. The PRIDE database and related tools and resources in 2019: improving support for quantification data. *Nucleic Acids Research* 47(D1):D442–D450.
- [52] Elias, J.E., Gygi, S.P., 2010. Target-decoy search strategy for mass spectrometry-based proteomics. *Methods in Molecular Biology* 604:55–71.
- [53] Vacic, V., Iakoucheva, L.M., Radivojac, P., 2006. Two Sample Logo: a graphical representation of the differences between two sets of sequence alignments. *Bioinformatics* 22(12):1536–1537.
- [54] Bloemberg, D., Quadrilatero, J., 2012. Rapid determination of myosin heavy chain expression in rat, mouse, and human skeletal muscle using multicolor immunofluorescence analysis. *PLoS One* 7(4):e35273.
- [55] Arbour, D., Tremblay, E., Martineau, E., Julien, J.P., Robitaille, R., 2015. Early and persistent abnormal decoding by glial cells at the neuromuscular junction in an ALS model. *Journal of Neuroscience* 35(2):688–706.
- [56] Tremblay, E., Martineau, E., Robitaille, R., 2017. Opposite synaptic alterations at the neuromuscular junction in an ALS mouse model: when motor units matter. *Journal of Neuroscience* 37(37):8901–8918.
- [57] Devries, M.C., Lowther, S.A., Glover, A.W., Hamadeh, M.J., Tarnopolsky, M.A., 2007. IMCL area density, but not IMCL utilization, is higher in women during moderate-intensity endurance exercise, compared with men. *American Journal of Physiology - Regulatory, Integrative and Comparative Physiology* 293(6):R2336–R2342.
- [58] Vincent, A.E., Ng, Y.S., White, K., Davey, T., Mannella, C., Falkous, G., et al., 2016. The spectrum of mitochondrial ultrastructural defects in mitochondrial myopathy. *Scientific Reports* 6:30610.
- [59] Hughes, M.C., Ramos, S.V., Turnbull, P.C., Rebalka, I.A., Cao, A., Monaco, C.M.F., et al., 2019. Early myopathy in Duchenne muscular dystrophy is associated with elevated mitochondrial H₂O₂ emission during impaired oxidative phosphorylation. *J Cachexia Sarcopenia Muscle* 10(3):643–661.
- [60] Buch, B.T., Halling, J.F., Ringholm, S., Gudiksen, A., Kjobsted, R., Olsen, M.A., et al., 2020. Colchicine treatment impairs skeletal muscle mitochondrial function and insulin sensitivity in an age-specific manner. *The FASEB Journal*.
- [61] Wang, X., Blagden, C., Fan, J., Nowak, S.J., Taniuchi, I., Littman, D.R., et al., 2005. Runx1 prevents wasting, myofibrillar disorganization, and autophagy of skeletal muscle. *Genes & Development* 19(14):1715–1722.
- [62] Mazzatti, D.J., Smith, M.A., Oita, R.C., Lim, F.L., White, A.J., Reid, M.B., 2008. Muscle unloading-induced metabolic remodeling is associated with acute alterations in PPARdelta and UCP-3 expression. *Physiological Genomics* 34(2):149–161.
- [63] Abadi, A., Glover, E.I., Isfort, R.J., Raha, S., Safdar, A., Yasuda, N., et al., 2009. Limb immobilization induces a coordinate down-regulation of mitochondrial and other metabolic pathways in men and women. *PLoS One* 4(8):e6518.
- [64] Ebert, A.D., Yu, J., Rose Jr., F.F., Mattis, V.B., Lorson, C.L., Thomson, J.A., et al., 2009. Induced pluripotent stem cells from a spinal muscular atrophy patient. *Nature* 457(7227):277–280.
- [65] Bialek, P., Morris, C., Parkington, J., St Andre, M., Owens, J., Yaworsky, P., et al., 2011. Distinct protein degradation profiles are induced by different disuse models of skeletal muscle atrophy. *Physiological Genomics* 43(19):1075–1086.
- [66] Festa, R.A., Jones, M.B., Butler-Wu, S., Sinsimer, D., Gerads, R., Bishai, W.R., et al., 2011. A novel copper-responsive regulon in *Mycobacterium tuberculosis*. *Molecular Microbiology* 79(1):133–148.
- [67] Jackman, R.W., Wu, C.L., Kandarian, S.C., 2012. The ChIP-seq-defined networks of Bcl-3 gene binding support its required role in skeletal muscle atrophy. *PLoS One* 7(12):e51478.
- [68] Sartori, R., Schirwis, E., Blaauw, B., Bortolanza, S., Zhao, J., Enzo, E., et al., 2013. BMP signaling controls muscle mass. *Nature Genetics* 45(11):1309–1318.
- [69] Macpherson, P.C., Farshi, P., Goldman, D., 2015. Dach2-Hdac9 signaling regulates reinnervation of muscle endplates. *Development* 142(23):4038–4048.
- [70] Chua, J.P., Reddy, S.L., Yu, Z., Giorgetti, E., Montie, H.L., Mukherjee, S., et al., 2015. Disrupting SUMOylation enhances transcriptional function and ameliorates polyglutamine androgen receptor-mediated disease. *Journal of Clinical Investigation* 125(2):831–845.
- [71] Haslett, J.N., Sanoudou, D., Kho, A.T., Bennett, R.R., Greenberg, S.A., Kohane, I.S., et al., 2002. Gene expression comparison of biopsies from Duchenne muscular dystrophy (DMD) and normal skeletal muscle. *Proceedings of the National Academy of Sciences of the United States of America* 99(23):15000–15005.
- [72] Osborne, R.J., Welle, S., Venance, S.L., Thornton, C.A., Tawil, R., 2007. Expression profile of FSHD supports a link between retinal vasculopathy and muscular dystrophy. *Neurology* 68(8):569–577.
- [73] Bachinski, L.L., Siritto, M., Bohme, M., Baggerly, K.A., Udd, B., Krahe, R., 2010. Altered MEF2 isoforms in myotonic dystrophy and other neuromuscular disorders. *Muscle & Nerve* 42(6):856–863.
- [74] Vihola, A., Bachinski, L.L., Siritto, M., Olufemi, S.E., Hajibashi, S., Baggerly, K.A., et al., 2010. Differences in aberrant expression and splicing of sarcomeric proteins in the myotonic dystrophies DM1 and DM2. *Acta Neuropathologica* 119(4):465–479.
- [75] Trollet, C., Anvar, S.Y., Venema, A., Hargreaves, I.P., Foster, K., Vignaud, A., et al., 2010. Molecular and phenotypic characterization of a mouse model of oculopharyngeal muscular dystrophy reveals severe muscular atrophy restricted to fast glycolytic fibres. *Human Molecular Genetics* 19(11):2191–2207.
- [76] Tedesco, F.S., Gerli, M.F., Perani, L., Benedetti, S., Ungaro, F., Cassano, M., et al., 2012. Transplantation of genetically corrected human iPSC-derived

- progenitors in mice with limb-girdle muscular dystrophy. *Science Translational Medicine* 4(140):140ra189.
- [87] Dadgar, S., Wang, Z., Johnston, H., Kesari, A., Nagaraju, K., Chen, Y.W., et al., 2014. Asynchronous remodeling is a driver of failed regeneration in Duchenne muscular dystrophy. *The Journal of Cell Biology* 207(1):139–158.
- [78] Thijssen, P.E., Balog, J., Yao, Z., Pham, T.P., Tawil, R., Tapscott, S.J., et al., 2014. DUX4 promotes transcription of FRG2 by directly activating its promoter in facioscapulohumeral muscular dystrophy. *Skeletal Muscle* 4:19.
- [79] Boscolo Sesillo, F., Fox, D., Sacco, A., 2019. Muscle stem cells give rise to rhabdomyosarcomas in a severe mouse model of duchenne muscular dystrophy. *Cell Reports* 26(3):689–701 e686.
- [80] Wang, E.T., Treacy, D., Eichinger, K., Struck, A., Estabrook, J., Olafson, H., et al., 2019. Transcriptome alterations in myotonic dystrophy skeletal muscle and heart. *Human Molecular Genetics* 28(8):1312–1321.
- [81] Lin, K.H., Wilson, G.M., Blanco, R., Steinert, N.D., Zhu, W.G., Coon, J.J., et al., 2021. A deep analysis of the proteomic and phosphoproteomic alterations that occur in skeletal muscle after the onset of immobilization. *Journal of Physiology* 599(11):2887–2906.
- [82] Wagner, S.A., Beli, P., Weinert, B.T., Scholz, C., Kelstrup, C.D., Young, C., et al., 2012. Proteomic analyses reveal divergent ubiquitylation site patterns in murine tissues. *Molecular & Cellular Proteomics* 11(12):1578–1585.
- [83] Leutert, M., Menzel, S., Braren, R., Rissiek, B., Hopp, A.K., Nowak, K., et al., 2018. Proteomic characterization of the heart and skeletal muscle reveals widespread arginine ADP-ribosylation by the ARTC1 ectoenzyme. *Cell Reports* 24(7):1916–1929 e1915.
- [84] Dhar, S., Vemulapalli, V., Patananan, A.N., Huang, G.L., Di Lorenzo, A., Richard, S., et al., 2013. Loss of the major Type I arginine methyltransferase PRMT1 causes substrate scavenging by other PRMTs. *Scientific Reports* 3:1311.
- [85] Larsen, S.C., Sylvestersen, K.B., Mund, A., Lyon, D., Mullari, M., Madsen, M.V., et al., 2016. Proteome-wide analysis of arginine monomethylation reveals widespread occurrence in human cells. *Science Signaling* 9(443).
- [86] Boisvert, F.M., Cote, J., Boulanger, M.C., Richard, S., 2003. A proteomic analysis of arginine-methylated protein complexes. *Molecular & Cellular Proteomics* 2(12):1319–1330.
- [87] Guo, A., Gu, H., Zhou, J., Mulhern, D., Wang, Y., Lee, K.A., et al., 2014. Immunoaffinity enrichment and mass spectrometry analysis of protein methylation. *Molecular & Cellular Proteomics* 13(1):372–387.
- [88] Bassel-Duby, R., Olson, E.N., 2006. Signaling pathways in skeletal muscle remodeling. *Annual Review of Biochemistry* 75:19–37.
- [89] Hoppeler, H., 2016. Molecular networks in skeletal muscle plasticity. *Journal of Experimental Biology* 219(Pt 2):205–213.
- [90] Sinha, A., Mann, M., 2020. A beginner's guide to mass spectrometry-based proteomics.
- [91] Hornbeck, P.V., Zhang, B., Murray, B., Kornhauser, J.M., Latham, V., Skrzypek, E., 2015. PhosphoSitePlus, 2014: mutations, PTMs and recalibrations. *Nucleic Acids Research* 43(Database issue):D512–D520.
- [92] Strahl, B.D., Allis, D., 2000. The language of covalent histone modifications. *Nature* 403.
- [93] Beltrao, P., Albanese, V., Kenner, L.R., Swaney, D.L., Burlingame, A., Villen, J., et al., 2012. Systematic functional prioritization of protein post-translational modifications. *Cell* 150(2):413–425.
- [94] Hendriks, I.A., Lyon, D., Young, C., Jensen, L.J., Vertegaal, A.C., Nielsen, M.L., 2017. Site-specific mapping of the human SUMO proteome reveals co-modification with phosphorylation. *Nature Structural & Molecular Biology* 24(3):325–336.
- [95] Parker, B.L., Kiens, B., Wojtaszewski, J.F.P., Richter, E.A., James, D.E., 2020. Quantification of exercise-regulated ubiquitin signaling in human skeletal muscle identifies protein modification cross talk via NEDDylation. *The FASEB Journal* 34(4):5906–5916.
- [96] Leutert, M., Entwisle, S.W., Villen, J., 2021. Decoding post-translational modification crosstalk with proteomics. *Molecular & Cellular Proteomics* 20:100129.
- [97] Kumar, P., Joy, J., Pandey, A., Gupta, D., 2017. PRmePRed: a protein arginine methylation prediction tool. *PLoS One* 12(8):e0183318.
- [98] Zheng, W., Wuyun, Q., Cheng, M., Hu, G., Zhang, Y., 2020. Two-Level Protein Methylation Prediction using structure model-based features. *Scientific Reports* 10(1):6008.
- [99] Cheng, D., Cote, J., Shaaban, S., Bedford, M.T., 2007. The arginine methyltransferase CARM1 regulates the coupling of transcription and mRNA processing. *Molecular Cell* 25(1):71–83.
- [100] Gayatri, S., Cowles, M.W., Vemulapalli, V., Cheng, D., Sun, Z.W., Bedford, M.T., 2016. Using oriented peptide array libraries to evaluate methylarginine-specific antibodies and arginine methyltransferase substrate motifs. *Scientific Reports* 6:28718.
- [101] Shishkova, E., Zeng, H., Liu, F., Kwiecien, N.W., Hebert, A.S., Coon, J.J., et al., 2017. Global mapping of CARM1 substrates defines enzyme specificity and substrate recognition. *Nature Communications* 8.
- [102] Li, W.J., He, Y.H., Yang, J.J., Hu, G.S., Lin, Y.A., Ran, T., et al., 2021. Profiling PRMT methylome reveals roles of hnRNPA1 arginine methylation in RNA splicing and cell growth. *Nature Communications* 12(1):1946.
- [103] Talbot, J., Maves, L., 2016. Skeletal muscle fiber type: using insights from muscle developmental biology to dissect targets for susceptibility and resistance to muscle disease. *Wiley Interdiscip Rev Dev Biol* 5(4):518–534.
- [104] Tintignac, L.A., Brenner, H.R., Ruegg, M.A., 2015. Mechanisms regulating neuromuscular junction development and function and causes of muscle wasting. *Physiological Reviews* 95(3):809–852.
- [105] Neukomm, L.J., Freeman, M.R., 2014. Diverse cellular and molecular modes of axon degeneration. *Trends in Cell Biology* 24(9):515–523.
- [106] Taetzsch, T., Valdez, G., 2018. NMJ maintenance and repair in aging. *Curr Opin Physiol* 4:57–64.
- [107] Rodriguez Cruz, P.M., Cossins, J., Beeson, D., Vincent, A., 2020. The neuromuscular junction in health and disease: molecular mechanisms governing synaptic formation and homeostasis. *Frontiers in Molecular Neuroscience* 13:610964.
- [108] Wan, J.J., Qin, Z., Wang, P.Y., Sun, Y., Liu, X., 2017. Muscle fatigue: general understanding and treatment. *Experimental and Molecular Medicine* 49(10):e384.
- [109] Tonino, P., Kiss, B., Strom, J., Methawasin, M., Smith 3rd, J.E., Kolb, J., et al., 2017. The giant protein titin regulates the length of the striated muscle thick filament. *Nature Communications* 8(1):1041.
- [110] Pedrotti, S., Giudice, J., Dagnino-Acosta, A., Knoblauch, M., Singh, R.K., Hanna, A., et al., 2015. The RNA-binding protein Rbfox1 regulates splicing required for skeletal muscle structure and function. *Human Molecular Genetics* 24(8):2360–2374.
- [111] Uhlen, M., Fagerberg, L., Hallstrom, B.M., Lindskog, C., Oksvold, P., Mardinoglu, A., et al., 2015. Tissue-based map of the human proteome. *Science* 347.
- [112] van der Pol, A., Gil, A., Tromp, J., Sillje, H.H.W., van Veldhuisen, D.J., Voors, A.A., et al., 2018. OPLAH ablation leads to accumulation of 5-oxoproline, oxidative stress, fibrosis, and elevated fillings pressures: a murine model for heart failure with a preserved ejection fraction. *Cardiovascular Research* 114(14):1871–1882.

- [113] Jager, S., Handschin, C., St-Pierre, J., Spiegelman, B.M., 2007. AMP-activated protein kinase (AMPK) action in skeletal muscle via direct phosphorylation of PGC-1alpha. *Proceedings of the National Academy of Sciences of the United States of America* 104(29):12017–12022.
- [114] Kjobsted, R., Hingst, J.R., Fentz, J., Foretz, M., Sanz, M.N., Pehmoller, C., et al., 2018. AMPK in skeletal muscle function and metabolism. *The FASEB Journal* 32(4):1741–1777.
- [115] Steinberg, G.R., Carling, D., 2019. AMP-activated protein kinase: the current landscape for drug development. *Nature Reviews Drug Discovery* 18(7):527–551.
- [116] Sandri, M., Lin, J., Handschin, C., Yang, W., Arany, Z.P., Lecker, S.H., et al., 2006. PGC-1alpha protects skeletal muscle from atrophy by suppressing FoxO3 action and atrophy-specific gene transcription. *Proceedings of the National Academy of Sciences of the United States of America* 103(44):16260–16265.
- [117] Handschin, C., Kobayashi, Y.M., Chin, S., Seale, P., Campbell, K.P., Spiegelman, B.M., 2007. PGC-1alpha regulates the neuromuscular junction program and ameliorates Duchenne muscular dystrophy. *Genes & Development* 21(7):770–783.
- [118] Chan, M.C., Arany, Z., 2014. The many roles of PGC-1alpha in muscle—recent developments. *Metabolism* 63(4):441–451.
- [119] Kim, D., Lim, S., Park, M., Choi, J., Kim, J., Han, H., et al., 2014. Ubiquitination-dependent CARM1 degradation facilitates Notch1-mediated podocyte apoptosis in diabetic nephropathy. *Cellular Signalling* 26(9):1774–1782.
- [120] Shin, H.J., Kim, H., Oh, S., Lee, J.G., Kee, M., Ko, H.J., et al., 2016. AMPK-SKP2-CARM1 signalling cascade in transcriptional regulation of autophagy. *Nature* 534(7608):553–557.
- [121] Zhou, K., Chen, H., Lin, J., Xu, H., Wu, H., Bao, G., et al., 2019. FGF21 augments autophagy in random-pattern skin flaps via AMPK signaling pathways and improves tissue survival. *Cell Death & Disease* 10(12):872.